Article

Coupling Controls the Synchrony of Clock Cells in Development and Knockouts

Isao T. Tokuda,[1,*] Daisuke Ono,[2] Bharath Ananthasubramaniam,[3] Sato Honma,[4] Ken-Ichi Honma,[4] and Hanspeter Herzel[5]

[1]Department of Mechanical Engineering, Ritsumeikan University, Shiga, Japan; [2]Photonic Bioimaging Section, Research Center for Cooperative Projects, Hokkaido University Graduate School of Medicine, Sapporo, Japan; [3]Institute for Theoretical Biology, Charité Universitätsmedizin, Berlin, Germany; [4]Department of Chronomedicine, Hokkaido University Graduate School of Medicine, Sapporo, Japan; and [5]Institute for Theoretical Biology, Humboldt University of Berlin, Berlin, Germany

ABSTRACT   In mammals, a network of coupled neurons within the hypothalamus coordinates physiological rhythms with daily changes in the environment. In each neuron, delayed negative transcriptional feedbacks generate oscillations, albeit noisy and unreliable ones. Coupling mediated by diffusible neuropeptides lends precision and robustness to circadian rhythms. The double knockout of Cryptochrome Cry turns adult mice arrhythmic. But, remarkably, double knockout neonates continue to show robust oscillation much like wild-type neonates and appear to lose rhythmicity with development. We study quantitatively dispersed neurons and brain slices from wild-type and Cry double knockout mice to understand the links between single cell rhythmicity and intercellular coupling. We quantify oscillator properties of dispersed cells using nonlinear regression and study bifurcations diagrams of network models. We find that varying just three parameters—oscillator strength, strength of coupling, and timing of coupling—can reproduce experimentally observed features. In particular, modeling reveals that minor changes in timing of coupling can destroy synchronization as observed in adult slices from knockout mice.

INTRODUCTION

A network of neurons in the suprachiasmatic nucleus (SCN) in the brain is primarily responsible for orchestrating temporal organization of most physiological processes in mammals (1). Using light inputs from the retina, this master circadian timekeeper adapts to diurnal and seasonal environmental changes (2). The network lends precision (3) and robustness (4) against certain genetic perturbations to this collection of ~20,000 noisy neuronal oscillators. The rhythms in gene transcription and firing in each neuron are generated by a delayed negative feedback involving certain clock genes, whose protein products repress their own transcription. It was, therefore, understood that clock genes accounted for rhythmicity in each neuron, while the intercellular signaling mediated by diffusible neuropeptides (5–7), synapses (8), and gap junctions worked to synchronize the network.

However, a recent study (9) revealed that a double knockout of clock genes, Cry1 and Cry2, disrupted synchrony in adult mice, while maintaining rhythmicity in single neurons. Remarkably, neonatal double knockout mice showed robust synchronized rhythms that appeared to deteriorate with development. These results question the current theory on the essential mechanisms necessary to achieve synchrony in the SCN, and leave the relative roles of single

cell rhythmicity and intercellular coupling open. We address this question by comparing SCNs from Cry1,2 knockout background (10) against wild-type (WT) SCN using an oscillator network modeling approach.

Modeling can help to identify generic mechanisms of synchronization from a wide variety of experimental data ranging from dispersed single cells and neonatal and adult SCN slice cultures, to perturbation of coupling and restoration of rhythm by coculturing. Date analysis highlights the high degree of heterogeneity in the periods, amplitudes, and degree of synchronization of different neurons within the SCN. Here, we study quantitatively six types of datasets: WT SCN (dispersed cells, neonatal and adult slices) and Cry double knockout (dispersed cells, neonatal and adult slices). Furthermore we perturb synchronization pharmacologically using TTX (tetrodotoxin). We find that the diversity of empirically observed behaviors can be reproduced in simulations by varying only three parameters. In addition, we can classify SCNs as strong and weak based on how easily they are synchronized to a global signal (11). Finally, we show that the timing of coupling is essential and provides a likely explanation of the changes in synchrony during development.

MATERIALS AND METHODS

Animals

CrossMark

PER2::LUC transgenic mice on the C57BL/6J background were used as the control. Mice were reared in the animal quarters in Hokkaido University where environmental conditions were controlled (lights-on, 6–18 h; light intensity, ~100 lx at the bottom of cage; humidity, 60 ± 10%). Experiments were conducted in compliance with the rules and regulations established by the Animal Care and Use Committee of Hokkaido University.

SCN slice and dispersed cell culture

For measurement of PER2::LUC bioluminescence from a cultured SCN slice, mice of 8–16 weeks or 2–5 days old kept under light-dark (LD) conditions were euthanized between 8 and 16 h by cervical dislocation and decapitated. The brain was rapidly removed and a coronal SCN slice of 100-μm thick for adults and 200 μm thick for neonates was made by a DTK-1000 D.S.K. microslicer (Dosaka EM, Kyoto, Japan) and a McIlwain tissue chopper (Ted Pella, Redding, CA), respectively. The brain slice containing the middle portion of the SCN was selected and trimmed ~2 × 2 mm square. The slice was cultured in air at 36.5°C with 1.2 mL Dulbecco's modified Eagle's medium (Invitrogen, Carlsbad, CA) with 0.2 mM D-luciferin K and 5% supplement solution, the composition of which was described previously in Ono et al. (9).

For the measurement of PER2::LUC from dispersed SCN cells, the SCNs from 4 to 8 neonatal pups (2–5 days old) were dissected from hypothalamic slices of 400-μm thick and dissociated using trypsin. Dispersed cells were plated on a 35-mm Petri dish precoated with 0.01% poly-L-ornithine. The cell density was 1100 ± 500 cells/mm^2. Medium composition was the same as that for slice culture, except for 5% fetal bovine serum in dispersed cell culture.

Bioluminescence imaging

Bioluminescence at the SCN cell level in cultured slices or in dispersed cells was obtained by a DM IRB (Leica Microsystems, Wetzlar, Germany), a Luminoview 200 (Olympus, Melville, NY), or a Cellgraph (Atto, Tokyo, Japan) equipped with an electron-multiplying charge-coupled device camera cooled at −80°C. Bioluminescence was measured every 60 min with an exposure time of 59 min for 7–14 days. The pixel size was 2.3 × 2.3 μm for the DM IRB, 2.0 × 2.0 μm for the Luminoview 200 (Olympus), and 1.6 × 1.6 μm for the Cellgraph (Atto). Bioluminescence signals were analyzed in terms of a region of interest (ROI). The mean area of a single ROI was ~100 μm^2, almost equivalent to the size of a single SCN cell. The intensity of bioluminescence was expressed as an average intensity of pixels involved in a ROI.

Actogram

Wheel-running activity was measured in a cage with a running-wheel (10 cm in diameter). Mice were individually housed in a polycarbonate cage placed in a light-proof box where environmental conditions were the same as in the animal quarters except for the light intensity in the light phase s (~300 1 ×). Wheel revolutions were fed into a computer every 1 min by computer software (The Chronobiology Kit; Stanford Software Systems, Stanford, CA).

Parameter estimation of single cell models

As a generic model for self-sustained oscillators, we introduce the following stochastic amplitude-phase oscillator (13):

$$\frac{dr}{dt} = \lambda(A - r) + \xi_r \quad (1)$$

$$\frac{d\varphi}{dt} = \omega + \xi_\varphi. \quad (2)$$

The system is described in polar coordinates of radius r and angle φ, and has a limit cycle with amplitude A and frequency ω. Any perturbation away from the limit cycle will relax back with a damping rate λ. The model has two noise intensities, one for amplitude fluctuations ($\langle \xi_r \rangle = 0$, $\langle \xi_r(t+\tau)\xi_r(t) \rangle = 2D_r\delta(\tau)$) and the other for phase noise ($\langle \xi_\varphi \rangle = 0$, $\langle \xi_\varphi(t+\tau)\xi_\varphi(t) \rangle = 2D_\varphi\delta(\tau)$). This model provides one of the simplest mathematical systems to generate limit cycle oscillations. Winfree (14) has studied this model in the context of circadian rhythms. It has been shown analytically that the stochastic system has an autocorrelation function in the following form (13):

$$C(\tau) = \frac{1}{2}\left(A^2 + \frac{D_r}{\lambda}e^{-\lambda\tau}\right)e^{-D_\varphi\tau}\cos\omega\tau. \quad (3)$$

The single cell model has five unknown parameters $\{A, \omega, \lambda, D_r, D_\varphi\}$ to be fitted to a dispersed cell culture data. The data fitting is performed as follows. First, the bioluminescence signal was detrended using a least-square fitting of a second-degree polynomial. The polynomial was then subtracted from the signal and the signal was mean centered. Next, the autocorrelation function was calculated from the detrended bioluminescence signal. We used only 40% of the autocorrelations representing the shortest time lags, because estimates of autocorrelations for larger time lags become poor. Then, the five parameters were optimized so that the autocorrelation function (Eq. 3) of the single cell model is fitted to that of the bioluminescence signal. We used the lsqcurvefit subroutine of the MATLAB Statistical Toolbox (The MathWorks, Natick, MA) to optimize the parameters. It should be noted that the fitting of Eq. 3 is an ill-conditioned problem, because the function involves a summation of two exponentials. To avoid misfitting, initial guesses are used as described in detail in Westermark et al. (13). From the estimated parameters, the coefficient of variation ($CV = \sigma_r/A = (\sqrt{D_r/\lambda})/A$) can be computed, which represents the ratio of the standard deviation of the amplitude fluctuations to the fit amplitude of a single cell oscillator. Note that the amplitude fluctuations can be directly computed as a function of the fitted parameters. Detailed steps of the parameter estimation, e.g., detrended bioluminescence signals, fitted autocorrelation functions, and simulated cellular signals, are shown in Fig. S1 in the Supporting Material. The effect of detrending on the estimation results is examined in Fig. S2.

Coupled amplitude-phase oscillators

We constructed a cellular network model of the SCN by coupling the amplitude-phase oscillators that were fitted previously to the single cell data. By studying synchronization property of the cellular network, we examined whether the dynamical characteristics of slice data can be reproduced. The single cell amplitude-phase model of Eqs. 1 and 2 was first transformed to Cartesian (x,y) coordinates (see Eqs. S1 and S2), whereupon interneuronal connections were introduced through x and y variables to obtain a network of SCN cells,

$$\frac{dx_i}{dt} = -\lambda_i\frac{x_i}{r_i}(r_i - A_i) + \omega_i y_i + K(\bar{x}_\psi - x_i) + \xi_{x,i} \quad (4)$$

$$\frac{dy_i}{dt} = -\lambda_i\frac{y_i}{r_i}(r_i - A_i) + \omega_i x_i + K(\bar{y}_\psi - y_i) + \xi_{y,i}, \quad (5)$$

where x_i and y_i represent dynamical variables of the ith cell ($i = 1, 2,..., N$), $\xi_{x,i}$ and $\xi_{y,i}$ are independent Gaussian noises, and $r_i = \sqrt{x_i^2 + y_i^2}$. A_i, ω_i, and λ_i are the parameters estimated previously. A global and diffusive coupling K with a coupling delay ψ is introduced with mean field coupling $\bar{x}_\psi = (1/N)\sum_{i=1}^{N}x_i(t-\psi)$ and $\bar{y}_\psi = (1/N)\sum_{i=1}^{N}y_i(t-\psi)$.

The degree of synchrony was quantified by means of the synchronization index R,

$$R = \frac{\langle\bar{x}^2\rangle - \langle\bar{x}\rangle^2}{\frac{1}{N}\sum_{i=1}^{N}\left(\langle x_i^2\rangle - \langle x_i\rangle^2\right)}, \quad (6)$$

where $\langle\cdots\rangle$ denotes the average over time, and $\bar{x} = (1/N)\sum_{i=1}^{N}x_i$ is the average of the variable of interest among oscillators.

Network model of biochemical oscillators

To evaluate the generality of our results beyond a network of coupled amplitude-phase oscillators, we constructed a network of more detailed biomechanical oscillators describing the individual cellular rhythms. We slightly modified a previously published model of coupled circadian oscillators that was used to study synchronization-induced rhythmicity (15). The intracellular model is composed of transcriptional/translational feedback loops of the core clock genes in the mammalian circadian system (16). The intercellular coupling in the SCN network is considered to be due to the circadian release of a neuropeptide. It is also assumed (15) that the release of the neuropeptide is induced quickly after the cytosolic PER/CRY protein complex. In the connected cells, the neuropeptide activates a signaling cascade of PKA and CREB, which then leads to activation of Per/Cry mRNA transcription. The dynamics of the single-cell oscillator is described by the following set of differential equations:

$$\frac{dY_1}{dt} = f_{\text{Per/Cry}} - k_{1d}Y_1 + L \tag{7}$$

$$\frac{dY_2}{dt} = k_{2b}Y_1^q - (k_{2d} + k_{2t})Y_2 + k_{3t}Y_3 \tag{8}$$

$$\frac{dY_3}{dt} = k_{2t}Y_2 - k_{3t}Y_3 - k_{3d}Y_3 \tag{9}$$

$$\frac{dY_4}{dt} = f_{\text{Bmal}} - k_{4d}Y_4 \tag{10}$$

$$\frac{dY_5}{dt} = k_{5b}Y_4 - (k_{5d} + k_{5t})Y_5 + k_{6t}Y_6 \tag{11}$$

$$\frac{dY_6}{dt} = k_{5t}Y_5 - (k_{6t} + k_{6d})Y_6 + k_{7a}Y_7 - k_{6a}Y_6 \tag{12}$$

$$\frac{dY_7}{dt} = k_{6a}Y_6 - (k_{7a} + k_{7d})Y_7 \tag{13}$$

$$\frac{dV}{dt} = k_8Y_2 - k_{8d}V \tag{14}$$

$$\frac{dX_1}{dt} = k_{x1}Q(X_{1T} - X_1) - k_{dx1}X_1 \tag{15}$$

$$\frac{dX_2}{dt} = k_{x2}X_1(X_{2T} - X_2) - k_{dx2}X_2. \tag{16}$$

The nonlinear transcription functions are given by

$$f_{\text{Per/Cry}} = v_{1b}\frac{Y_7 + X_2^h}{k_{1b}\left(1 + (Y_3/k_{1i})^p\right) + \left(Y_7 + X_2^h\right)} \tag{17}$$

$$f_{\text{Bmal}} = v_{4b}\frac{Y_3^r}{k_{4b}^r + Y_3^r}. \tag{18}$$

The variables represent the following species: Y_1, Per/Cry mRNA; Y_2, PER/CRY cytosolic complex; Y_3, nuclear PER/CRY complex; Y_4, Bmal1 mRNA; Y_5, cytosolic BMAL1; Y_6, nuclear BMAL1; Y_7, transcriptionally active BMAL1*; V, neuropeptide; X_1, PKA; and X_2, CREB.

Parameter configurations in biochemical models are usually not known in detail. To cope with such ambiguity, parameter values for the single cell model were chosen from two published studies: one as a model of a self-sustained oscillator (16) and the other as a model of a damped oscillator (15). There two parameter sets varied only in the parameters representing $P = \{p, k_{2t}, k_{4b}, k_{1d}, k_{2d}, k_{3d}, k_{4d}, k_{5d}, k_{6d}, k_{7d}\}$ and the corresponding parameter values are termed P_1 for the self-sustained oscillator (16) and P_2 for the damped oscillator (15) with values listed in Table S2. The remaining model parameters were held at fixed values listed in Table S3.

By introducing a parameter representing oscillator strength α ($0 \leq \alpha \leq 1$) that linearly interpolates between the two oscillatory regimes as

$$P = \alpha P_1 + (1 - \alpha)P_2, \tag{19}$$

we simulate the effect of Cry1 and Cry2 double deficiency. The cells of knockout mice can be characterized by $\alpha = 0$, which gives rise to a strongly damped oscillation. On the other hand, a larger value of α leads to a regime of self-sustained oscillation (see Fig. S4 a). It should be noted that there is no direct biochemical interpretation of the parameter variation of α, because the intracellular models are not quantitative in all details.

To simulate a network of N cellular oscillators, the single cell model was replicated N times (for readability, the indices $i = 1,\ldots,N$ for X and Y variables were omitted). To add heterogeneity, each set of equations is scaled by a factor $e_i = 0.92/g_i$ to generate a distribution of periods, where g_i is generated from a Gaussian distribution centered at 1 with a standard deviation of 0.05. This 5% period spread was arrived at as a consensus of our estimated period variability from single cell analysis and several published estimates (3,17,18).

The coupling function Q, which activates two-step signaling cascade leading to Per/Cry mRNA transcription, is given by $Q = KF(t - \psi)$, where F is a mean field of the neuropeptide, K determines the coupling strength, and ψ represents the coupling delay. As an average concentration of the neuropeptide released by the SCN cells, the mean field is given by $F = (1/N)\sum_{i=1}^{N}V_i$. Among a variety of SCN network topologies that have been considered (15,19–22), only the case of global coupling was considered as the simplest yet reasonable representation based on the globally diffusive nature of the neuropeptide.

To take into account the effect of molecular noise, stochastic dynamics of the circadian system was simulated based on the chemical Langevin equation (23). The light input was simulated by the following clipped sine wave,

$$L(t) = \begin{cases} L_0 \sin\left(\dfrac{\pi t \bmod T}{T}\right) & \text{if } t \bmod T < 0.5T, \\ 0 & \text{otherwise,} \end{cases} \tag{20}$$

where L_0 is the Zeitgeber intensity and T is the Zeitgeber period.

RESULTS

Oscillator network modeling requires appropriate single cell models (16,24,25) together with reasonable assumptions on network topology and coupling mechanisms (15,26,27). As a first step, we extract from the dispersed cell cultures single cell parameters (periods, amplitudes, and noise strength) using regression analysis. The distributions of these single cell parameters allow suitable parameterization of previously published gene regulatory network models. WT cells are identified as self-sustained oscillators, whereas $Cry1^{-/-}/Cry2^{-/-}$ cells are well represented by noise-driven damped

oscillators. By comprehensively varying coupling strength and coupling delay, we can specify parameter regions with synchronized rhythms. It turns out that varying just three parameters—oscillator strength α, coupling strength K, and coupling delay ψ—can reproduce experimentally observed features. Next, we describe our results in detail.

Extracting single cell parameters

Data for single cell parameter estimation was drawn from PER2::LUC bioluminescence recordings of plated SCN slices as described in Nakamura et al. (28) (see Materials and Methods). In total, we analyzed $N = 74$ WT cells and $N = 48$ cells from double knockout $Cry1^{-/-}/Cry2^{-/-}$ mice, each measured every 60 min for 7–14 days (Figs. 1, S8, and S9). Using nonlinear regression, introduced by Westermark et al. (13) and outlined in the Materials and Methods, we estimated for each cell a period T, amplitude A, relaxation rate λ, and fluctuation strength D_r by fitting a stochastic amplitude-phase model. Representative traces of the fits to individual cells and their reproduction by our stochastic model are shown in Fig. S1. $N = 66$ WT cells and $N = 14$ knockout $Cry1^{-/-}/Cry2^{-/-}$ cells fit the model reasonably well. Of particular interest is the coefficient of variation (CV) representing fluctuations in the amplitude relative to the mean amplitude. For $CV > 1$, the associated stationary probability densities are unimodal and the cells can be regarded as noise-driven damped oscillators (13).

Fig. 1 and Table 1 show key results of our regression: the periods of WT cells center at ~24 h and almost half of them exhibit $CV < 1$. This implies that these cells are relatively

reliable oscillators and can be classified theoretically as noisy limit-cycle oscillators. On the contrary, the estimated periods of $Cry1^{-/-}/Cry2^{-/-}$ cells vary in the range from 20 to 40 h and all CV values exceed 1. Consequently, cells from knockout mice are much less reliable oscillators and can be regarded as noise-driven damped oscillators. These findings were robust to the use of raw or detrended bioluminescence data for single cell parameter estimation (see Fig. S2).

In summary, there is a spectrum of oscillators from limit-cycle oscillators that are reliable and have continued rhythmicity without stimulation to damped oscillators that lose rhythm amplitude. This spectrum can be parameterized by the CV under our regression approach (13) and allows us to classify cells from different genotypes. These findings serve as constraints on more complex simulations of gene regulatory networks presented next.

Simulations of coupled amplitude-phase oscillators

We next coupled the amplitude-phase oscillators fit to the dispersed cell data from the previous section according to Eqs. 4 and 5 to study the network dynamics of this simple SCN model. The network consisted of $N = 66$ and $N = 14$ parameterized cells with reasonable fits to dispersed cells in WT and double knockout $Cry1^{-/-}/Cry2^{-/-}$ mice, respectively. Fig. 2 shows dependencies of the network synchrony on the coupling strength K and coupling delay ψ for WT and double knockout cell networks. For the coupled oscillators constructed from WT cells, synchrony clearly appears as the coupling strength is increased. Interestingly, the
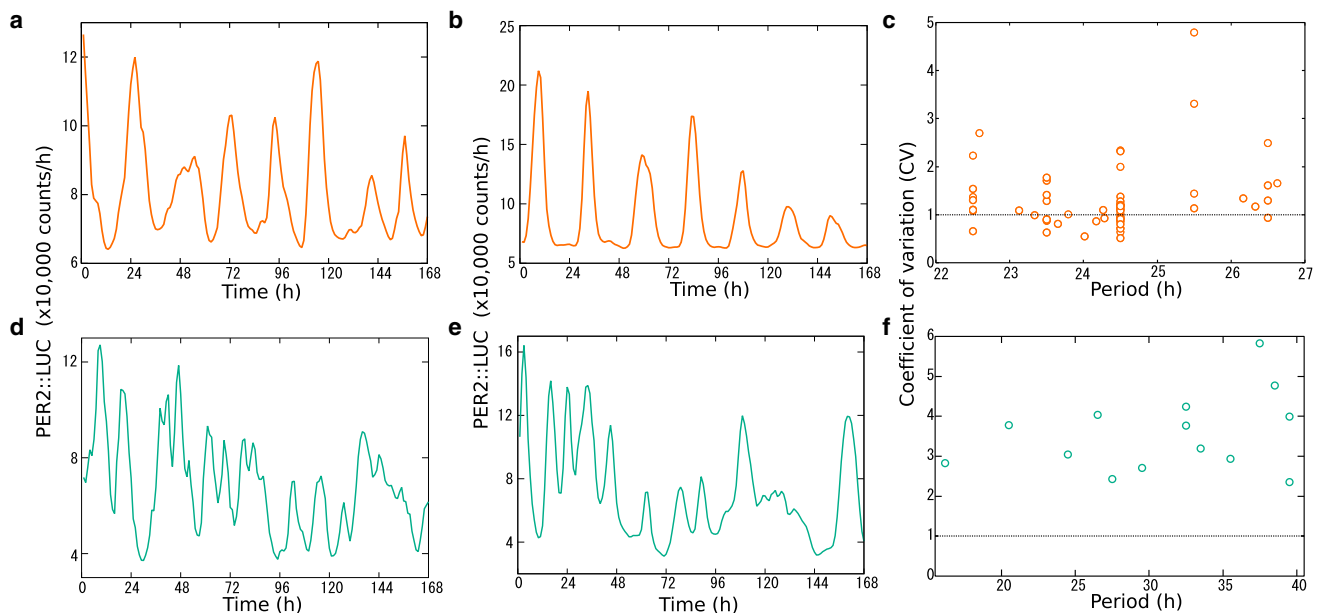

FIGURE 1 Analysis of oscillations in dispersed SCN cell cultures. Sample bioluminescence traces from dispersed SCN cell culture from WT (*a* and *b*) and knockout ($Cry1^{-/-}/Cry2^{-/-}$) mice (*d* and *e*). Single cell analyses of biolumininescene traces from dispersed cell culture of WT ($N = 66$) (*c*) and knockout ($N = 14$) SCNs (*f*). Abscissa and ordinate represent estimated period and coefficient of variation CV, respectively. To see this figure in color, go online.

TABLE 1 Results of the single cell analysis for dispersed culture data of WT ($N = 74$) and double knockout mice ($Cry1^{-/-}/Cry2^{-/-}$, $N = 48$)

	Mouse	Period (h)	Cells with $CV < 1$ (%)
Experiment	WT	24.3 ± 1.1	36.4
	$Cry1^{-/-}/Cry2^{-/-}$	31.1 ± 7.3	0
Model	WT	19.6 ± 1.6	39.5
	$Cry1^{-/-}/Cry2^{-/-}$	32.7 ± 6.7	6.7

The estimated values are compared with those of the simulation data. Average and standard deviation of the estimated period $T = 2\pi/\omega$ are indicated and the percentage of rhythmic cells having a $CV < 1$ is shown.

synchronization depends upon the coupling delay ψ. Although a small coupling delay enhances the synchronization, a medium coupling delay at ~$\psi = 12$ h destroys the synchronization. It has been known in coupled phase oscillators that the effect of coupling can easily turn from attractive to repulsive by a coupling delay of half of the intrinsic period (29). The observed desynchrony can be understood as a result of such repulsive (or negative) coupling. A similar basic structure can be observed in the synchronization diagram of the network constructed from knockout cells (Fig. 2 b). Compared to the network of WT cells, the region of synchronization in the network of $Cry1^{-/-}/Cry2^{-/-}$ cells is smaller and, moreover, the level of synchrony (measured by the synchronization index) is not as high even with a strong coupling and a small coupling delay. This is likely due to the increased heterogeneity and higher noise in the double knockout cells that therefore necessitate stronger coupling to induce global synchrony.

As a possible default situation for neonate slices, the coupling strength and delay were set as $K = 0.1$ and $\psi = 0$ h and for adult slice, the delay was increased to $\psi = 5.5$ h. Under these conditions, the model simulations

(Fig. S3) capture essential features of the bioluminescence data seen later in Fig. 5. In other words, the coupling was strong enough to synchronize both WT and knockout cells in neonate slice. Introduction of the coupling delay of $\psi = 5.5$ h in the adult slice maintained the synchrony in the WT cells, whereas it destroyed the synchrony in the knockout cells. Next, administration of TTX to adult slice was simulated by reducing the coupling strength from $K = 0.1$ to 0.04 at time $t = 72$ h (see Fig. S3, c and f). Whereas the WT cells maintained the synchronized oscillations even after the TTX administration, the phases of the double knockout cells started to move apart from each other, resulting in desynchronized oscillations during TTX administration.

Simulations of gene-regulatory circadian oscillators

The simulations of coupled amplitude-phase oscillators revealed that coupling strength and delay have major effects on the synchronization properties of the network. Moreover, clear differences between WT and knockout mice were visible. Next, we examined whether these observations are valid also in a more detailed gene-regulatory network model developed in earlier studies (15,16). The model is based on transcriptional-translational feedback loops involving the transcription factor BMAL1 and the PER/CRY complex (see Fig. 3 a). The effects of light input and coupling are included via the upregulation of transcription. It has been shown that the diffusible neuropeptide VIP plays an essential role in synchronizing SCN neurons (5,7,30). Therefore, we implemented global coupling of all SCN neurons in our model using a mean field representing the average neuropeptide level in the extracellular medium (Fig. 3 b).
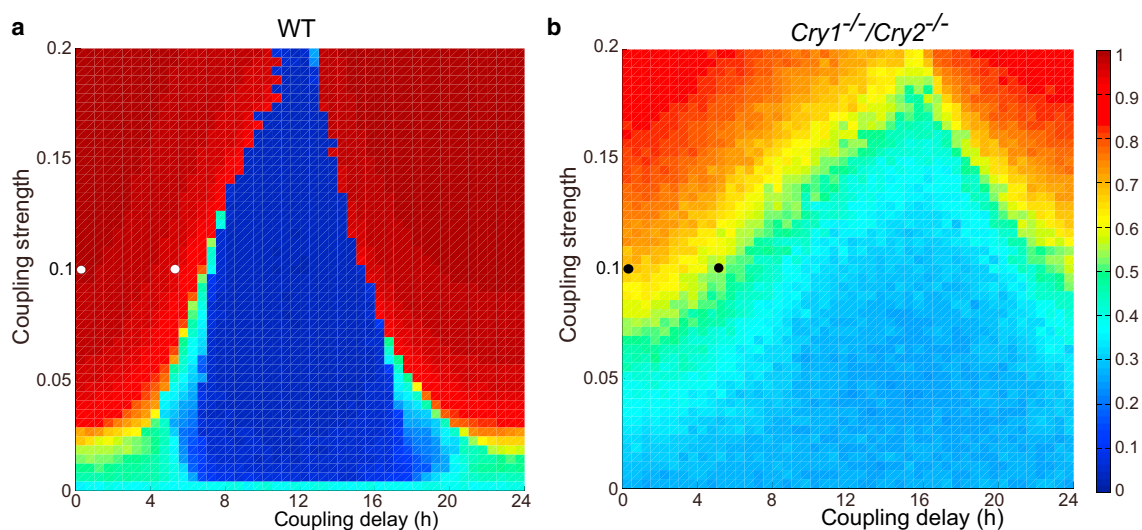

FIGURE 2 Dependence of the synchronization index R of the coupled amplitude-phase model on the coupling strength K and coupling delay ψ. (*Open and solid points*) Where the simulated $Cry1^{-/-}/Cry2^{-/-}$ and WT SCN mice in Fig. S3, respectively, lie. The models were parameterized using fits to dispersed WT (*a*) and $Cry1^{-/-}/Cry2^{-/-}$ SCN cells (*b*). To see this figure in color, go online.
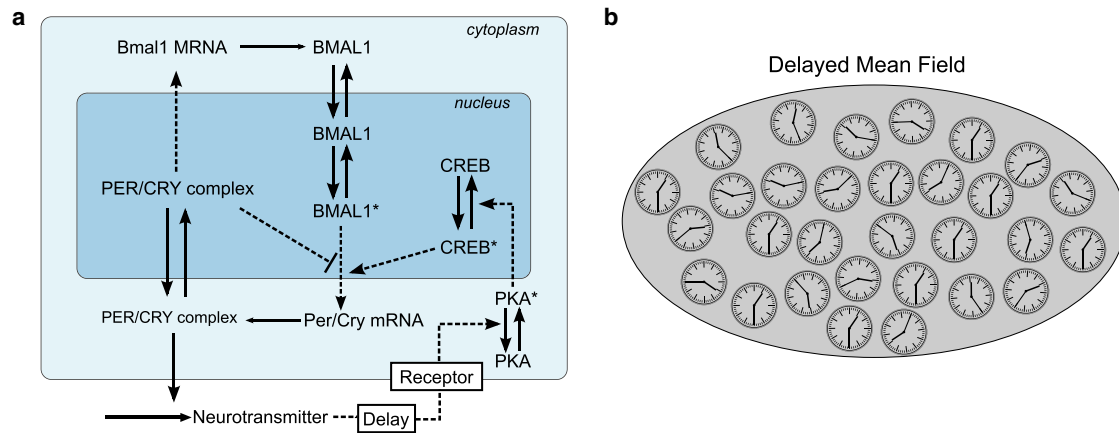
FIGURE 3 Schematic of the single cell oscillator and the coupled SCN network. (*a*) The intracellular model consists of transcriptional/translational feedback loops of clock genes, modified from Bernard et al. (15). Clock genes induce the release of a neuropeptide that acts as a coupling agent. Feedback of the neuropeptide activates PKA and CREB, leading to Per/Cry mRNA transcription. (*b*) The individual cellular oscillators are coupled through a mean field of the released neuropeptide in the intercellular medium with a time delay to account for different phases of neuropeptide release. To see this figure in color, go online.

To keep the number of adjusted parameters small, we introduce, in addition to the coupling strength and its delay, to our knowledge, a novel parameter α that characterizes the strength of an oscillator in the network. The gene-regulatory network model was originally developed to describe self-sustained single cell oscillations (16). A modified version was used subsequently to generate damped single cell oscillations (15). Our single cell analyses have shown that many WT cells exhibit self-sustained rhythms, whereas $Cry1^{-/-}/Cry2^{-/-}$ appear to be damped. As a parameter to control such single cell property, the oscillator strength α interpolates between the two parameter sets published earlier (15,16). The corresponding bifurcation diagram shows a smooth transition from damped to self-sustained oscillations in Fig. S4. For knockout cells, we chose $\alpha = 0$ and for WT cells $\alpha = 0.3$. The omnipresent molecular noise, for example, induced by transcriptional bursts (31), is taken into account by stochastic simulation based on the chemical Langevin equation (23).

We then examined ability of the resulting simulations in Fig. 4 to reproduce qualitatively the bioluminescence SCN dispersed cell data in Fig. 1. The simulated traces in Fig. 4 represent noisy signals with no clear periodicity as observed in the bioluminescence data. For a quantitative comparison of experimental data and simulations, we applied our nonlinear regression approach also to the simulated data. Table 1 and Fig. 4, *c* and *f* (compare Fig. 1, *c* and *f*), demonstrate that simulations reproduce the most essential properties of dispersed WT and knockout $Cry1^{-/-}/Cry2^{-/-}$ SCN cells.

Strength and timing of coupling control synchronization

Our SCN slice data from WT and $Cry1^{-/-}/Cry2^{-/-}$ mice show different degrees of synchronization depending on the degree of development of the mice (see Figs. 5 and S10–S13 and Table S1). For example, neonatal knockout mice exhibit robust synchronization that deteriorates with development. To find possible explanations for this variability, we employ network simulations of our gene-regulatory model. We systematically vary the single cell oscillator strength α, coupling strength K, and its coupling delay ψ. The timing of coupling, parameterized by ψ, depends on the expression profiles of neuropeptides and their receptors. There are reports of oscillating levels of VIP and its receptor VPAC2 (32,33). These observations suggest that intracellular regulation can control cell-to-cell coupling. Consequently, clock knockout mice or mice at different developmental stages might exhibit different coupling strengths and timing.

We quantify the degree of synchrony by the synchronization index R (see Eq. 6). Fig. 6, *a* and *b* and show the index R for comprehensive variations of the core model parameters α, K, and ψ. To clarify the regime of damped oscillations, periodicity is drawn for the same parameter variations in Fig. S5. Oscillator strength α and coupling parameters K and ψ have profound effects on the degree of synchronization, as observed for the amplitude-phase oscillator networks. Interestingly, damped single cell oscillators (small α) are particularly easy to synchronize with each other as described earlier (15,26). As expected, large coupling strength K increases the synchronization index. More surprisingly, the timing of coupling described by ψ also has a very strong effect on synchronization, as shown in Ananthasubramaniam et al. (34).

We mark in Fig. 6, *a* and *b*, specific parameter configurations that reproduce qualitative experimental findings. That is, the simulated neonate WT and $Cry1^{-/-}/Cry2^{-/-}$ network display synchrony, while on development to an adult, the WT network remains synchronous, whereas the double
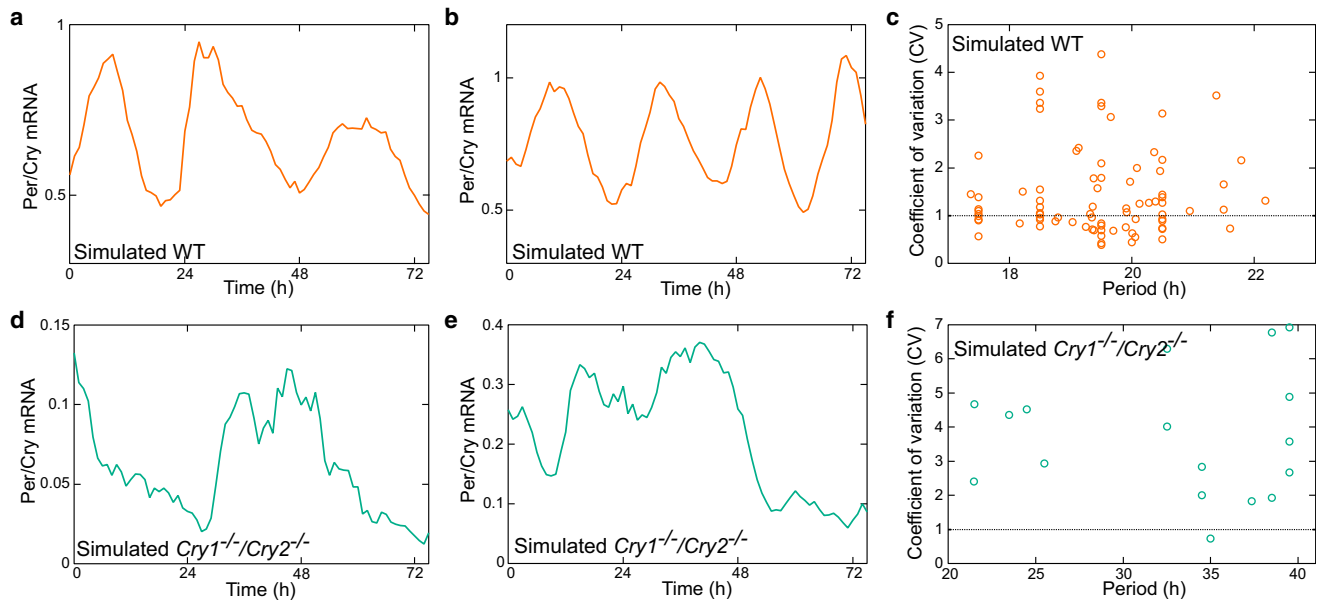
FIGURE 4 Analysis of oscillations in simulated SCN dispersed cell cultures. Sample simulated signals for dispersed SCN cells from WT (*a* and *b*) ($\alpha = 0$, $K = 0.2$, $\psi = 0$) and knockouts (*d* and *e*) ($\alpha = 0.3$, $K = 0.2$, $\psi = 0$). Single cell characteristics of simulated dispersed cells for WT (*c*) and knockout (*f*) are shown. Abscissa and ordinate represent estimated period and coefficient of variation *CV*, respectively. To see this figure in color, go online.

knockout is desynchronous. Oscillator strength $\alpha = 0.3$ and $\alpha = 0$ represent WT and double knockout mice, respectively. $K = 1$ describes slice data well, whereas very small K values, such as $K = 0.2$, mimic dispersed cultures better. While there is no evidence that coupling strength changes with development, preliminary data indicate that VIP expression profiles vary with age (32). Our simulations

show that an increase of ψ from zero to 12 h can deteriorate synchronization.

Comparison of network simulations in Fig. 7 with experimental data presented in Fig. 5 demonstrate that by varying just three parameters—oscillator strength α, coupling strength K, and coupling delay ψ—we can mimic complex experimental findings.
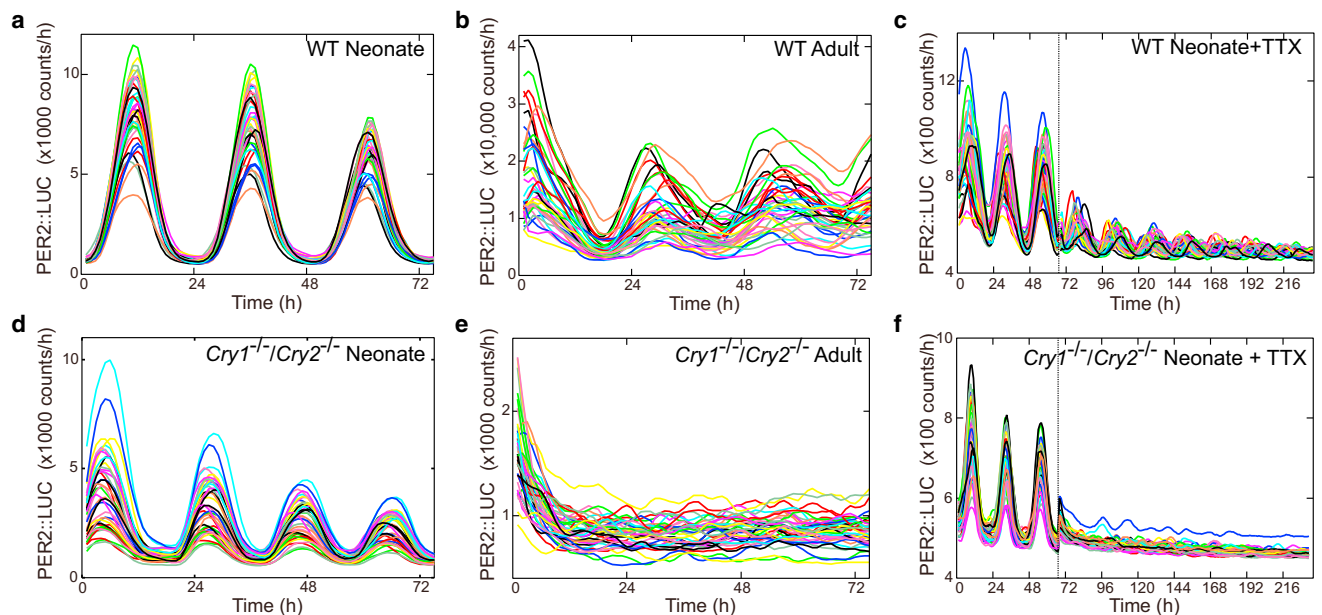

FIGURE 5 Comparison of single cell bioluminescence signals from SCN slice culture across genotype, age, and pharmacological perturbation. Bioluminescence signals from SCN slice culture of WT mouse from neonate (*a* and *c*) and adult (*b*). (*Dashed line* in *c*) Timing at which TTX was administered to a neonate slice. The corresponding bioluminescent signal traces for the knockout mouse are shown in (*d*)–(*f*). To see this figure in color, go online.
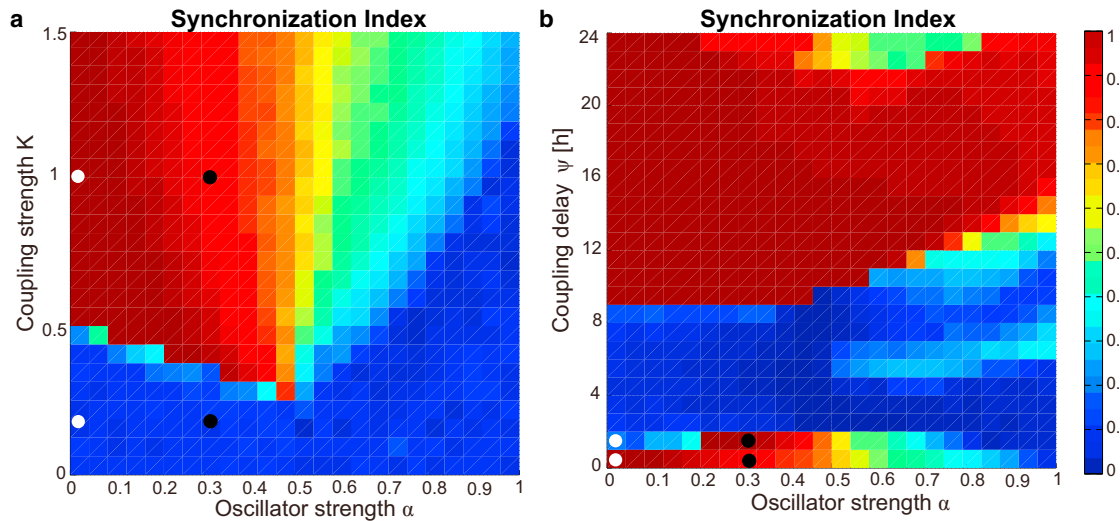
FIGURE 6 Oscillator synchrony in the simulated SCN for different choices of system parameters. (*a*) Dependence of the synchronization index *R* of the cellular network model on the oscillator strength α and coupling strength *K*. (*Open* and *solid points*) Conditions for simulating $Cry1^{-/-}/Cry2^{-/-}$ and WT mice, respectively, in Fig. 7. (*b*) Dependence of the synchronization index *R* on single cell oscillator strength α and the coupling delay ψ (coupling strength was set to $K = 1$). To see this figure in color, go online.

Weak oscillator networks have a wide entrainment range

So far, we studied synchronization in the absence of external LD cycles. Under natural conditions, Zeitgebers entrain endogenous circadian rhythms allowing adaptation to environmental cycles. Entrainment of WT mice is illustrated in Fig. 8 *a*. There is a precise onset of activity at the beginning of the dark phase. After release in continuous darkness (DD)

the onset of activity is shifted to an earlier time every day, indicating an intrinsic period below 24 h.

Interestingly, knockout mice can also be entrained by LD cycles (10,35) as shown in Fig. 8 *b*. These features can be reproduced by our network simulation as illustrated in Fig. 8, *c* and *d*. The agreement of experiments and simulations is illustrated by periodograms in Figs. S6 and S7.

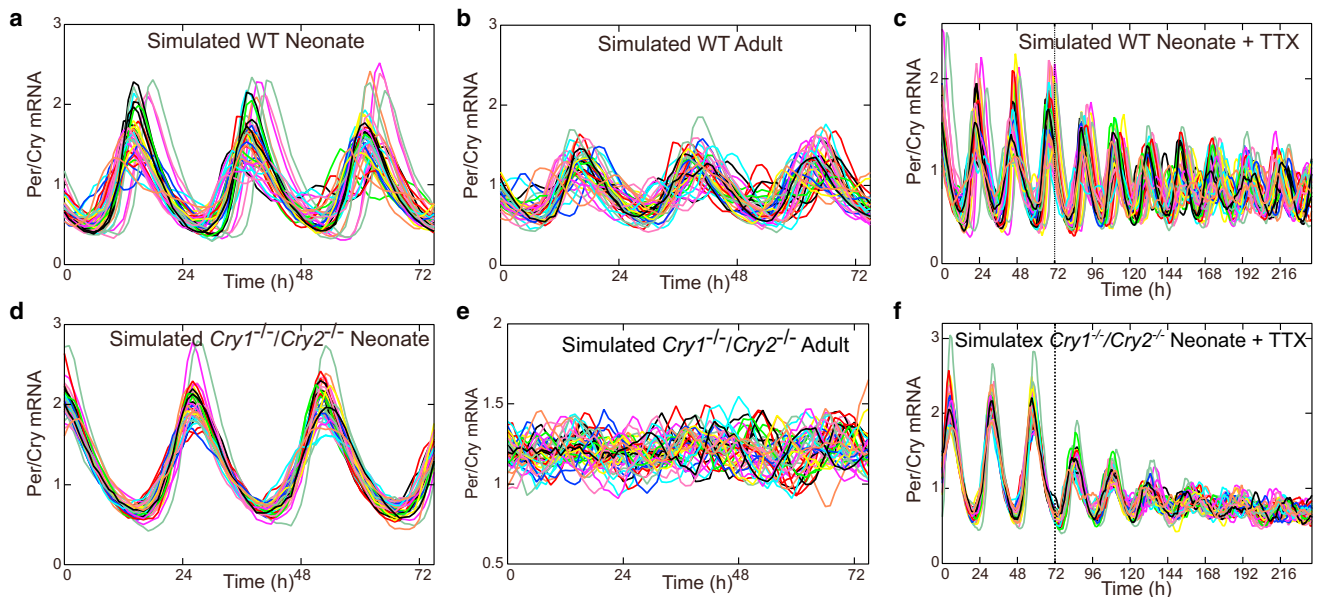It was suggested in the preceding section that adult $Cry1^{-/-}/Cry2^{-/-}$ mice have impaired coupling. It has

FIGURE 7 Comparison of SCN cellular network model across genotype, age, and pharmacological perturbation (corresponding to Fig. 5). (*a–c*) Simulated clock mRNA levels in the SCN network of WT mouse ($\alpha = 0.3$, $K = 1$). (*a* and *c*) Neonates ($\psi = 0$); (*b*) adults ($\psi = 1$). (*Dashed line* in *c*) Time at which the coupling was lowered from $K = 1$ to $K = 0.4$ simulating administration of tetrodotoxin. (*d–f*) The corresponding clock mRNA levels in the SCN network of a $Cry1^{-/-}/Cry2^{-/-}$ mouse ($\alpha = 0$, $K = 1$). The neonate ($\psi = 0$) is shown in (*d*) and (*f*) and adults ($\psi = 1$) in (*f*). To see this figure in color, go online.
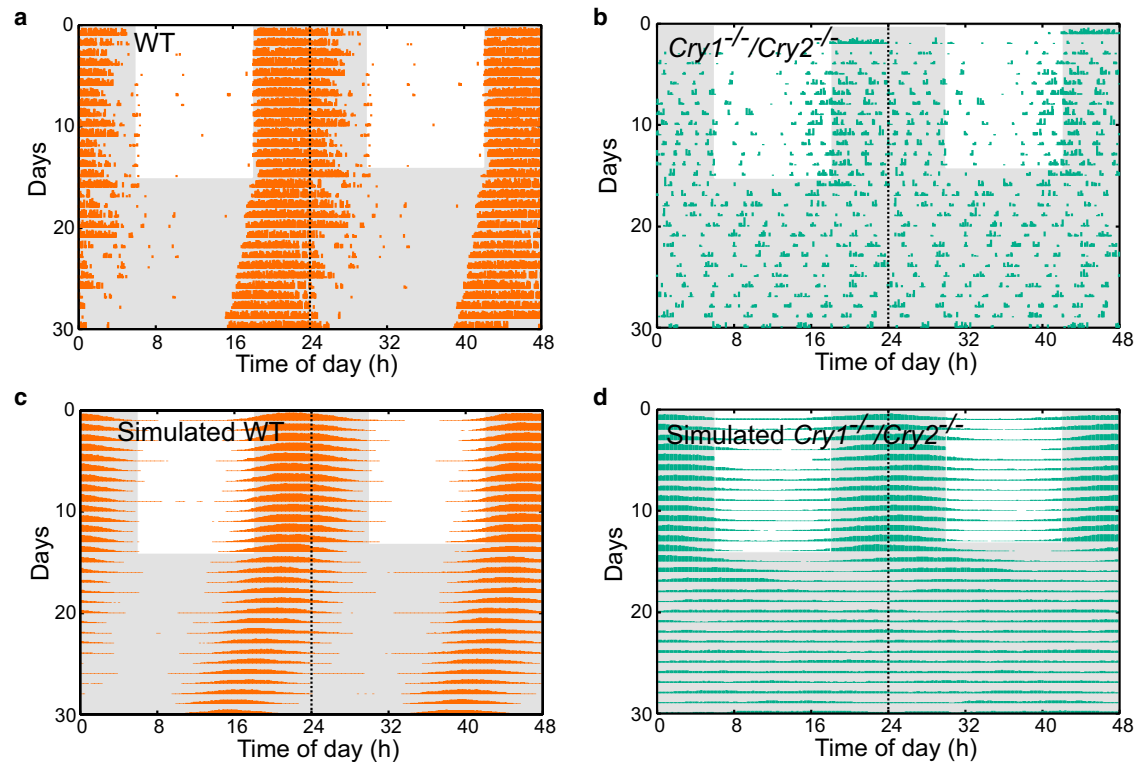
FIGURE 8 Comparison of behavioral rhythms in mice from both genotypes against simulated predictions. (*a*) Actogram of WT mouse, which was initially put under LD condition and then exposed to DD condition. (*b*) Actogram of knockout mouse ($Cry1^{-/-}/Cry2^{-/-}$), which was initially put under LD condition and then exposed to DD condition. (*c*) Simulated actogram corresponding to the WT mouse in (*a*). (*d*) Simulated actogram corresponding to the knockout mouse in (*b*). To see this figure in color, go online.

been shown previously (36) that weak coupling increases the range of entrainment, i.e., the range of external periods to which entrainment can be achieved. Fig. 9 demonstrates that our network simulations of knockout mice have indeed a much larger range of entrainment. These modeling results have been confirmed by experimental observations (37). Consequently, the SCN of knockouts can be regarded as a weak oscillator (see Granada et al. (11) for mathematical classifications of weak and strong oscillators), which is characterized by a large range of entrainment.

DISCUSSION

Our study was motivated by the inability of current theories based on compartmentalized mechanisms for rhythm generation and intercellular coupling to explain the complex phenotypes displayed by dispersed cells and SCN slices in WT and knockout mice. In particular, the robust synchronous rhythms of neonatal slices with disrupted rhythm generation components in $Cry1^{-/-}/Cry2^{-/-}$ mice and the subsequent loss of synchrony in adult slices, while maintaining single cell rhythms, was difficult to interpret. Our data-driven modeling connects rhythmicity of single cells to synchronous rhythms in a population of cells via intercellular coupling.

As a starting point, we applied regression techniques based on Westermark et al. (13) to dispersed neurons from WT and double knockout mice from Ono et al. (9). We thus quantified cellular oscillators from different genotypes as damped or self-sustained based on rhythm regularities. Consistent with earlier analyses (13,18,38) using different data, we concluded that there are, in fact, a continuum of single cell oscillator characteristics between self-sustained and damped oscillators. These results guided our parameter
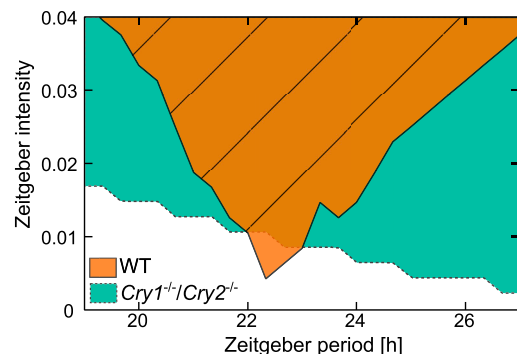

FIGURE 9 Dependence of the entrainment range of the network model to Zeitgeber parameters. The combinations of Zeitgeber period T and intensity L_0 for which the network model entrains to the Zeitgeber is shown for WT and $Cry1^{-/-}/Cry2^{-/-}$. To see this figure in color, go online.

determination in more complex models capable of connecting single cell rhythmicity and the release of coupling agents, such as the neuropeptide VIP, to the SCN network.

Because single cell data do not support a strict classification into damped and self-sustained oscillators, we varied systematically a system parameter α quantifying the strength of the single cell oscillators. This allowed us to distinguish weak oscillators and strong oscillators along the lines of Granada et al. (11) and Abraham et al. (36). Interestingly, damped oscillators that are considered weak can be more easily synchronized and exhibit wide entrainment ranges. Varying coupling strength K and coupling delay ψ in a network with reasonable single cell characteristics, we find that both parameters govern the synchrony of the network. Even minor changes in timing of the neuropeptide release led to complete loss of synchrony. Our findings allowed us to reproduce the complexity of observations by varying just three parameters: oscillator strength α, coupling strength K, and coupling delay ψ. Because both coupled amplitude-phase oscillators and coupled gene regulatory oscillators showed essentially the same results, our findings appeared to be model-independent.

In particular, our results suggest that the observed loss of synchrony from neonates to adults in knockout mice can be explained by changes in just these three system properties. As seen in Fig. 10, the experimental data (WT versus $Cry1^{-/-}/Cry2^{-/-}$, neonate versus adult, dispersed cells versus slice culture) can be located in a space spanned by the three parameters. Our data-driven analysis showed that the strength of oscillators is weaker in knockout than in WT mice. Reduction of the coupling strength in slices produced desynchronized oscillators as observed in dispersed cells (compare Fig. 4 and Fig. 6 a). While the amplitude and period of the SCN appears to change with age (39), there is no direct evidence of implicating changes in strength of coupling.

A novel model-based suggestion is that the coupling delay (or timing of coupling) ψ changes with age. Along with changes in the timing of neuropeptide release with age, knockout of two core clock components $Cry1,2$ possibly affects the phase of neuropeptide release, which is under clock control (40). Therefore, the knockout SCN having weak single oscillators is severely disrupted with development, whereas the WT is not. There is indeed evidence in rats that shows that circadian phase of VIP mRNA changes with age (32).

This hypothesis is the explanation of other counterintuitive observations described recently in Evans et al. (41). Many studies suggest that GABA acts in the SCN as a desynchronizer opposing the synchronization via VIP and gap junctions (42). However, in the case of SCN regions being out of phase, GABA contributes to resynchronization (41). A plausible explanation of these seemingly contradictory facts might be the distinct phase of GABA release.

Network simulations discussed in this article provide a framework to integrate details of intracellular dynamics with coupling mechanisms including relative timing of coupling. The predicted phenotype with a small change in the timing of coupling points to the need for empirically measuring the timing (or phase) of important coupling agents, such as VIP and AVP, under in vitro or in vivo conditions in both neonates and adults, building on the work of Ban et al. (32). Moreover, this marked phenotype might cause the timing to be evolutionarily selected. Based on the predicted role of timing of coupling, we propose experimental investigation of the effect of time-of-day dependent perturbation of coupling agents and their receptors. Finally, circadian changes in coupling might play a role in seasonal adaptation of the circadian system (20,43,44) and tuning the phase angle of entrainment (11,45).

SUPPORTING MATERIAL

Supporting Materials and Methods, thirteen figures, and three tables are available at http://www.biophysj.org/biophysj/supplemental/S0006-3495(15)00995-9.

AUTHOR CONTRIBUTIONS

H.P.H., B.A., I.T.T., S.H., and K.I.H. designed the study; D.O. performed the experiments; I.T.T. analyzed the data and simulated models; and I.T.T., B.A., D.O., and H.P.H. wrote the text.
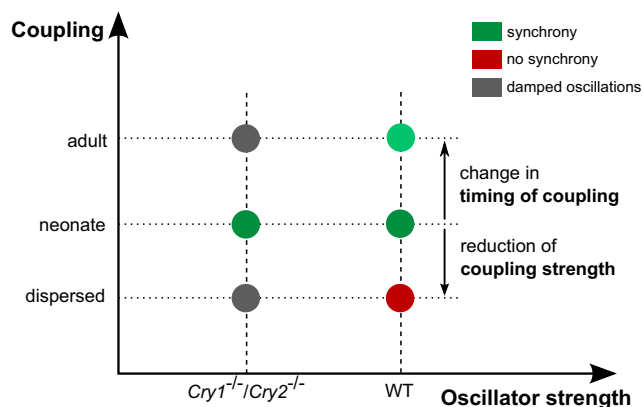
ACKNOWLEDGMENTS

FIGURE 10 Schematic illustration of the mechanism of coupling-induced rhythmicity. Abscissa represents system parameter that controls the single oscillator properties (WT versus knockout). Ordinate represents developmental stage (adult versus neonate), in which the coupling properties (e.g., coupling strength K or coupling delay ψ) are changed. To see this figure in color, go online.

SUPPORTING CITATIONS

References (46,47) appear in the Supporting Material.

REFERENCES

1. Welsh, D. K., J. S. Takahashi, and S. A. Kay. 2010. Suprachiasmatic nucleus: cell autonomy and network properties. *Annu. Rev. Physiol.* 72:551–577.

2. Herzog, E. D. 2007. Neurons and networks in daily rhythms. *Nat. Rev. Neurosci.* 8:790–802.

3. Herzog, E. D., S. J. Aton, …, H. Tei. 2004. Temporal precision in the mammalian circadian system: a reliable clock from less reliable neurons. *J. Biol. Rhythms.* 19:35–46.

4. Liu, A. C., D. K. Welsh, …, S. A. Kay. 2007. Intercellular coupling confers robustness against mutations in the SCN circadian clock network. *Cell.* 129:605–616.

5. Aton, S. J., C. S. Colwell, …, E. D. Herzog. 2005. Vasoactive intestinal polypeptide mediates circadian rhythmicity and synchrony in mammalian clock neurons. *Nat. Neurosci.* 8:476–483.

6. Maywood, E. S., A. B. Reddy, …, M. H. Hastings. 2006. Synchronization and maintenance of timekeeping in suprachiasmatic circadian clock cells by neuropeptidergic signaling. *Curr. Biol.* 16:599–605.

7. Maywood, E. S., J. E. Chesham, …, M. H. Hastings. 2011. A diversity of paracrine signals sustains molecular circadian cycling in suprachiasmatic nucleus circuits. *Proc. Natl. Acad. Sci. USA.* 108:14306–14311.

8. Yamaguchi, S., H. Isejima, …, H. Okamura. 2003. Synchronization of cellular clocks in the suprachiasmatic nucleus. *Science.* 302:1408–1412.

9. Ono, D., S. Honma, and K. Honma. 2013. Cryptochromes are critical for the development of coherent circadian rhythms in the mouse suprachiasmatic nucleus. *Nat. Commun.* 4:1666.

10. van der Horst, G. T., M. Muijtjens, …, A. Yasui. 1999. Mammalian Cry1 and Cry2 are essential for maintenance of circadian rhythms. *Nature.* 398:627–630.

11. Granada, A. E., G. Bordyugov, …, H. Herzel. 2013. Human chronotypes from a theoretical perspective. *PLoS One.* 8:e59464.

12. Yoo, S.-H., S. Yamazaki, …, J. S. Takahashi. 2004. PERIOD2:LUCIFERASE real-time reporting of circadian dynamics reveals persistent circadian oscillations in mouse peripheral tissues. *Proc. Natl. Acad. Sci. USA.* 101:5339–5346.

13. Westermark, P. O., D. K. Welsh, …, H. Herzel. 2009. Quantification of circadian rhythms in single cells. *PLOS Comput. Biol.* 5:e1000580.

14. Winfree, A. T. 2001. The Geometry of Biological Time. Springer, New York.

15. Bernard, S., D. Gonze, …, A. Kramer. 2007. Synchronization-induced rhythmicity of circadian oscillators in the suprachiasmatic nucleus. *PLOS Comput. Biol.* 3:e68.

16. Becker-Weimann, S., J. Wolf, …, A. Kramer. 2004. Modeling feedback loops of the mammalian circadian oscillator. *Biophys. J.* 87:3023–3034.

17. Welsh, D. K., D. E. Logothetis, …, S. M. Reppert. 1995. Individual neurons dissociated from rat suprachiasmatic nucleus express independently phased circadian firing rhythms. *Neuron.* 14:697–706.

18. Webb, A. B., N. Angelo, …, E. D. Herzog. 2009. Intrinsic, nondeterministic circadian rhythm generation in identified mammalian neurons. *Proc. Natl. Acad. Sci. USA.* 106:16493–16498.

19. Fukuda, H., I. Tokuda, …, N. Hayasaka. 2011. Quantitative analysis of phase wave of gene expression in the mammalian central circadian clock network. *PLoS One.* 6:e23568.

20. Bodenstein, C., M. Gosak, …, M. Perc. 2012. Modeling the seasonal adaptation of circadian clocks by changes in the network structure of the suprachiasmatic nucleus. *PLOS Comput. Biol.* 8:e1002697.

21. Hafner, M., H. Koeppl, and D. Gonze. 2012. Effect of network architecture on synchronization and entrainment properties of the circadian oscillations in the suprachiasmatic nucleus. *PLOS Comput. Biol.* 8:e1002419.

22. Vasalou, C., E. D. Herzog, and M. A. Henson. 2009. Small-world network models of intercellular coupling predict enhanced synchronization in the suprachiasmatic nucleus. *J. Biol. Rhythms.* 24:243–254.

23. Gillespie, D. T. 2000. The chemical Langevin equation. *J. Chem. Phys.* 113:297–306.

24. Leloup, J.-C., and A. Goldbeter. 2003. Toward a detailed computational model for the mammalian circadian clock. *Proc. Natl. Acad. Sci. USA.* 100:7051–7056.

25. Forger, D. B., and C. S. Peskin. 2003. A detailed predictive model of the mammalian circadian clock. *Proc. Natl. Acad. Sci. USA.* 100:14806–14811.

26. Gonze, D., S. Bernard, …, H. Herzel. 2005. Spontaneous synchronization of coupled circadian oscillators. *Biophys. J.* 89:120–129.

27. To, T.-L., M. A. Henson, …, F. J. Doyle, 3rd. 2007. A molecular model for intercellular synchronization in the mammalian circadian clock. *Biophys. J.* 92:3792–3803.

28. Nakamura, W., S. Honma, …, K. Honma. 2002. Clock mutation lengthens the circadian period without damping rhythms in individual SCN neurons. *Nat. Neurosci.* 5:399–400.

29. Kuramoto, Y. 1984. Chemical Oscillations, Waves, and Turbulence. Springer, Berlin, Germany.

30. Reed, H. E., A. Meyer-Spasche, …, H. D. Piggins. 2001. Vasoactive intestinal polypeptide (VIP) phase-shifts the rat suprachiasmatic nucleus clock in vitro. *Eur. J. Neurosci.* 13:839–843.

31. Suter, D. M., N. Molina, …, F. Naef. 2011. Mammalian genes are transcribed with widely different bursting kinetics. *Science.* 332:472–474.

32. Ban, Y., Y. Shigeyoshi, and H. Okamura. 1997. Development of vasoactive intestinal peptide mRNA rhythm in the rat suprachiasmatic nucleus. *J. Neurosci.* 17:3920–3931.

33. An, S., C. Tsai, …, E. D. Herzog. 2012. Spatiotemporal distribution of vasoactive intestinal polypeptide receptor 2 in mouse suprachiasmatic nucleus. *J. Comp. Neurol.* 520:2730–2741.

34. Ananthasubramaniam, B., E. D. Herzog, and H. Herzel. 2014. Timing of neuropeptide coupling determines synchrony and entrainment in the mammalian circadian clock. *PLOS Comput. Biol.* 10:e1003565.

35. Ono, D., S. Honma, and K. Honma. 2013. Postnatal constant light compensates Cryptochrome1 and 2 double deficiency for disruption of circadian behavioral rhythms in mice under constant dark. *PLoS One.* 8:e80615.

36. Abraham, U., A. E. Granada, …, H. Herzel. 2010. Coupling governs entrainment range of circadian clocks. *Mol. Syst. Biol.* 6:438.

37. Honma, S., D. Ono, and K. Honma. 2014. Cellular oscillators in the suprachiasmatic nucleus for behavior rhythm expression in the mouse lacking cryptochrome. *In* Dynamics of Circadian Oscillation in the SCN. K. Honma, editor. Hokkaido University Press, Sapporo, Hokkaido, Japan, pp. 85–96.

38. Rougemont, J., and F. Naef. 2007. Dynamical signatures of cellular fluctuations and oscillator stability in peripheral circadian clocks. *Mol. Syst. Biol.* 3:93.

39. Yamazaki, S., M. Straume, …, G. D. Block. 2002. Effects of aging on central and peripheral mammalian clocks. *Proc. Natl. Acad. Sci. USA.* 99:10801–10806.

40. Shinohara, K., S. Honma, …, K. Honma. 1994. Circadian rhythms in the release of vasoactive intestinal polypeptide and arginine-vasopressin in organotypic slice culture of rat suprachiasmatic nucleus. *Neurosci. Lett.* 170:183–186.

41. Evans, J. A., T. L. Leise, …, A. J. Davidson. 2013. Dynamic interactions mediated by nonredundant signaling mechanisms couple circadian clock neurons. *Neuron.* 80:973–983.

42. Freeman, G. M., Jr., R. M. Krock, …, E. D. Herzog. 2013. GABA networks destabilize genetic oscillations in the circadian pacemaker. *Neuron.* 78:799–806.

43. Pfeuty, B., Q. Thommen, …, M. Lefranc. 2012. Circadian clocks in changing weather and seasons: lessons from the picoalga *Ostreococcus tauri. BioEssays.* 34:781–790.

44. Azzi, A., R. Dallmann, …, S. A. Brown. 2014. Circadian behavior is light-reprogrammed by plastic DNA methylation. *Nat. Neurosci.* 17:377–382.

45. Bordyugov, G., U. Abraham, …, H. Herzel. 2015. Tuning the phase of circadian entrainment. *J. R. Soc. Interface.* 12:20150282.

46. Halberg, F., Y. Tong, and E. Johnson. 1967. Circadian system phase, an aspect of temporal morphology; procedures and illustrative examples. *In* The Cellular Aspects of Biorhythms. H. von Mayersbach, editor. Springer, Berlin, Germany, pp. 20–48.

47. Sokolove, P. G., and W. N. Bushell. 1978. The χ^2 periodogram: its utility for analysis of circadian rhythms. *J. Theor. Biol.* 72:131–160.

Supporting Material
Coupling controls synchrony of clock cells in development and knockouts

Isao T. Tokuda, Daisuke Ono, Bharath Ananthasubramaniam,
Sato Honma, Ken-Ichi Honma, Hanspeter Herzel

This supplementary material presents detailed numerical procedures for simulations of mathematical model of the cellular network model and analyses of experimental and simulation data. It contains ten sections: (1) amplitude-phase modeling of dispersed data, (2) network of coupled amplitude-phase models, (3) quantification of slice data, (4) Hopf bifurcation of the single cell model, (5) dependence of network dynamics on system parameters, (6) entrainment of network dynamics to external stimuli, (7) simulation of actograms, (8) analysis of slice culture data, (9) detailed parameter setting for the biochemical model, (10) additional samples of bioluminescence signals.

1   Amplitude-phase modeling of dispersed data

Taking two examples of dispersed cell culture data (one from wild-type and the other from knockout mouse), this section provides basic procedures of fitting the amplitude equation model to the experimental data. First, bioluminescence signal $\{x(t) : t = 1, 2, \ldots, T\}$ recorded from dispersed cell of neonate SCN slice was detrended using a least square fitting of a second-degree polynomial. The polynomial was subtracted from the signal so that the signal was mean centered. The detrended signal was the normalized in such a way that the signal has zero mean and unit variance. Figs. S1, *a* and *d*, represent detrended and normalized signals from the raw data of Fig. 1, *a* and *d*, respectively.

Second, with respect to the normalized signal $x(t)$, the autocorrelation $C(k)$ (with the time lag of k sampling intervals) was computed as

$$C(k) = \frac{1}{M-k}\sum_{i=1}^{M-k}(x_i - \bar{x}_0)(x_{i+k} - \bar{x}_k) \tag{S1}$$

where M is the number of samples in the time-series, and $\bar{x}_0 = \frac{1}{M}\sum_{i=1}^{M}x_i$ and $\bar{x}_k = \frac{1}{M-k}\sum_{i=1}^{M-k}x_{i+k}$ represent the mean values. The autocorrelation function detects periodicity in the signal $x(t)$, where the time lag that points to the first peak roughly corresponds to the period length of the signal.

Third, parameters of the stochastic amplitude-phase model of Eq. 1 were estimated by fitting the model to the experimental data. The single cell model has five unknown parameters $\{A, \omega, \lambda, D_r, D_\varphi\}$ to be fitted to the dispersed cell culture data. As described in the main text, the single cell model has an autocorrelation function defined by Eq. 3. The five parameters were optimized so that the autocorrelation function of the single cell model is fitted to that of the bioluminescence signal. We used `lsqcurvefit` subroutine of the MATLAB Statistical Toolbox to optimize the parameters. It should be noted that the fitting of Eq. 3 may face the problem of local minima, since the function involves a summation of two exponentials, which may create redundancy. To avoid miss-fitting, initial guesses were used as described in detail in [1]. Figs. S1, c and f, compare autocorrelation function $C(k)$ of the experimental data and that of the fitted model. The model captures basic feature of the experimental curve fairly well. From the estimated parameters, the intrinsic period and the coefficient of variation were obtained as $T = 2\pi/\omega$ and $\mathrm{CV} = \sigma_r/A = (\sqrt{D_r/\lambda})/A$. For the experimental data shown in Figs. 1, a and d (corresponding to Figs. S1, a and d), they were estimated as $T = 22.5$ h, $\mathrm{CV} = 1.3$ for the wild-type cell and $T = 33.5$ h, $\mathrm{CV} = 3.2$ for the knockout cell.

The same procedure was repeated for dispersed culture data of wild-type cells ($N = 74$) and $Cry1^{-/-}/Cry2^{-/-}$ cells ($N = 48$). $N = 66$ WT cells and $N = 14$ knockout cells were fitted to the model reasonably well. The results are summarized in Figs. 1, c and f, where estimated CV is plotted against estimated period $T = 2\pi/\omega$. Compared to the wild-type, the period was distributed more broadly in the knockoutm. As summarized in Table. 1, the mean and the standard deviation were 24.3±1.1 h for the wild-type and 31.1±7.3 h for the knockout. Of special note is that, if the CV is greater than 1, probability density of the state variables of the oscillator becomes qualitatively the same as that of a damped oscillator. However, if the CV is less than 1, it can be characetrized as a self-sustained oscillator. Hence, $CV = 1$ provides a criterion to distinguish self-sustained oscillators from damped oscillators. Among the wild-type cells, 36.4% of the neurons were characterized as self-sustained oscillators (textiti.e., CV < 1), whereas no cell were classified into self-sustained oscillators in the knockout cells.

Finally, the effect of detrending on the data was examined. In the studies of circadian rhythms, the detrending has been widely utilized as a postprocessing of the measurement data. Since our method focuses on existence of a limit cycle oscillation around the origin, the signal detrending, which introduces changes to oscillation amplitude, may influence the results. Fig. S2 summarizes the results of single cell analysis without detrending of the data. Compared with Figs. 1, c and f, the overall structure remains the same. As anticipated, the CV range is slightly increased, because the trend component, which exists in the raw data and was not removed by the detrending, might have hidden the oscillatory structure in the signal amplitude. The estimated period was 24.2±1.1 h for the wild-type cells and 26.8±7.0 h for the knockout cells. Among the wild-type cells, 7.2% of the cells were characterized as self-sustained oscillators, whereas no cells were classified into self-sustained oscillators. Compared to the results with

detrended data, the period estimates remained almost the same. Concerning the percentile of the self-sustained oscillators, it decreased in the non-detrended WT data. This is becase large portion of the WT cells is located around the critical line (CV = 1) and the slight shift in CV moved the cells to region of noisy oscillators (textiti.e., CV > 1).

We consider that the effect of the detrending does not influence our conclusion, since essentially the same features remained to distinguish $Cry1^{-/-}/Cry2^{-/-}$ cells from wild-type cells. Alternative criterion, which is less sensitive to a small shift in CV, should be further developed to characterize self-sustained oscillators.
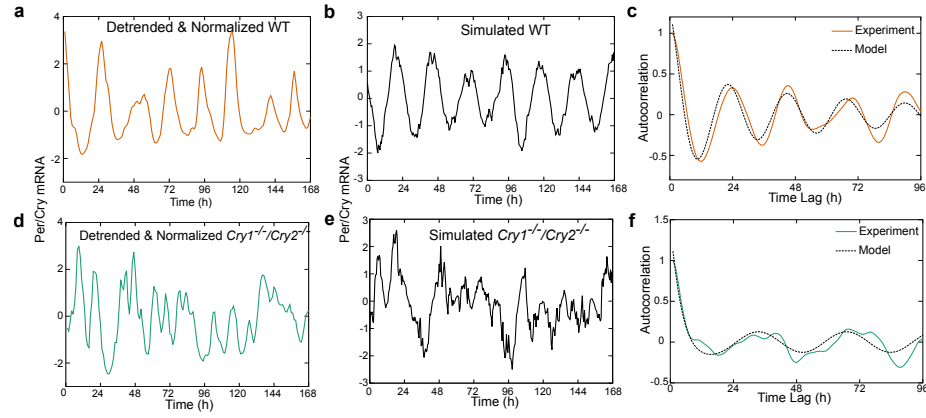

Figure S1: Procedure for parameter estimation. **a**, **d**: Detrended and normalized signals. **b**, **e**: Simulated signal by the stochastic amplitude model with estimated parameters. **c**, **f**: Autocorrelation functions of the experimental data (red solid line: WT, green solid line: knockout) and model (black dotted line).
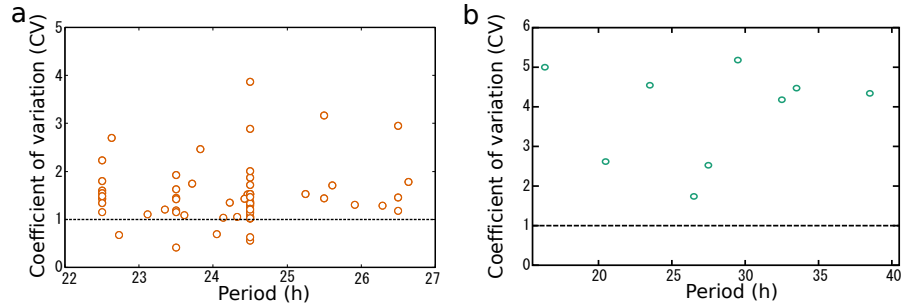

Figure S2: Single cell analyses of biolumninescence signals from dispersed cell culture without detrending. Abscissa and ordinate represent estimated period and coefficient of variation CV, respectively. (**a**): wild-type ($N = 69$). (**b**): knockout ($N = 10$).

2 Network of coupled amplitude-phase models

In this section, we construct a network of amplitude-phase models, each of which was fitted to dispersed cellular data in the previous section. By studying the network dynamics, we examine whether macroscopic properties such as dynamical characteristics of the slice data can be reproduced by the model. In particular, we focuse on the synchronization property of the cellular network.

The single cell model of the stochastic amplitude-phase equations 1-2 can be represented in Cartesian (x, y)-coordinates as

$$\frac{dx}{dt} = -\lambda \frac{x}{r}(r - A) + \omega y + \xi_x, \tag{S2}$$

$$\frac{dx}{dt} = -\lambda \frac{y}{r}(r - A) + \omega x + \xi_y, \tag{S3}$$

where ξ_x and ξ_y are independent Gaussian noises and $r = \sqrt{x^2 + y^2}$. By applying interneuronal connections though x and y variables, a network of SCN cells was constructed as Eqs. 4-5. The coupling is characterized by the strength K and delay ψ. From the data fitting detained in the previous section, we obtained N single cell models, whose parameters $(\lambda_i, A_i, \omega_i)$ correspond to the dispersed cellular data well. Such parameters were used to construct a network composed of $N = 66$ and $N = 14$ neurons for the wild-type and knockout mice, respectively.

Fig. 2 shows dependence of the network synchrony on the coupling strength K and coupling delay ψ. The level of synchrony was measured by the synchronization index $R = \frac{<\bar{x}^2> - <\bar{x}>^2}{\frac{1}{N}\sum_{i=1}^{N}(<x_i^2> - <x_i>^2)}$ as defined by Eq. 6. $< \cdots >$ denotes average over time and $\bar{X} = \frac{1}{N}\sum_{i=1}^{N} X_i$ is the average of x-variables among N oscillators. For the network of amplitude oscillators, whose parameter values were extracted from the WT cells (Fig. 2a), clear synchrony appears as the coupling strength is increased. Interestingly, the synchronization depends upon the coupling delay ψ. Although a small delay enhances the synchronization, a medium delay around $\psi = 12$ h destroys the synchronization. It has been known in coupled phase oscillators that the coupling force can be easily turned repulsive by a shift of half of the intrinsic period. The observed desynchrony can be understood as a result of such repulsive coupling. Similar structure can be observed in the synchronization diagram of the network constructed from knockout cells (Fig. 2b). Compared to the case of WT cells, the regime of synchronization is smaller. Moreover, the level of synchrony is not so high even with a strong coupling and a small coupling delay. This is due to the extended heterogeneity of the knockout cells, which require stronger coupling to induce global synchrony. Higher level of noise also disturbed the synchronized cellular activities.

For fixed coupling strength and delay, traces of the cellular activities coupled were drawn in Fig. S3. The simulated models capture essential features of the bioluminescence data of Fig. 5. Setting the coupling strength and delay as $K = 0.1$ and $\psi = 0$ h, default situation for neonate slice was established.

4

Under the default setting, networks of both WT and knockout cells generated synchronized cellular activities. Introduction of the delay of $\psi = 5.5$ h maintained the synchrony in the WT cells, whereas it destroyed the synchrony in the knockout cells. Such features closely resemble the adult slices of Figs. 5, *b* and *e*. To simulate the administration of tetrodotoxin (TTX), the coupling strength was reduced from $K = 0.1$ to $K = 0.04$ at time $t = 72$ h in Figs. S3, *c* and *f*. Whereas the WT cells maintained the synchronized oscillations even after the TTX, phases of the knockout cells started to get apart from each other, resulting in a desynchronized oscillations after the TTX. These reproduce qualitative features of the TTX experiment of Figs. 5, *c* and *f*, very well.

To summarize, the network of coupled amplitude equations simulated essential features of the experimental data. The coupling strength K and delay ψ may play a key role in organizing the slice activities as well as in inducing a developmental change from neonate to adult. This agrees with our results of network of biochemical models (Eqs. 7-18) composed of transcriptional/translational feedback loops of the core clock genes simulated in the main text. Our conclusion that variation of the three parameters (*i.e.*, individual oscillator characteristics, strength of coupling, and timing of coupling) suffices to reproduce experimental data is general, largely independent of the choice of the oscillator models.
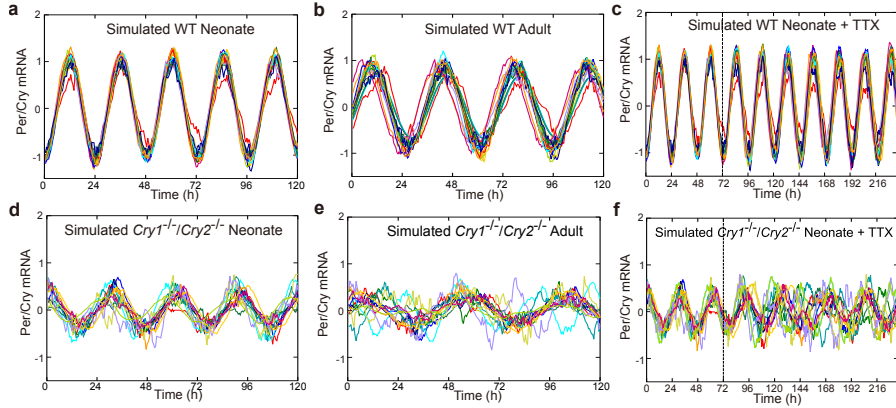

Figure S3: Simulation of coupled amplitude equation models corresponding to Fig. 5. **a,b,c**: Network of amplitude models constructed from wild-type (WT) SCN cells ($K = 0.1$). (**a,c**) and (**b**) represent neonates ($\psi = 0$), and adults ($\psi = 5.5$h), respectively. The dashed line in (**c**) indicates the time at which the coupling was lowered from $K = 0.1$ to $K = 0.04$ simulating administration of tetrodotoxin. **d,e,f**: Network of amplitude models constructed from $Cry1^{-/-}/Cry2^{-/-}$ mouse ($K = 0.1$). The neonate ($\psi = 0$) is shown in (**d,f**) and adults ($\psi = 5.5$h) in (**f**).

3 Quantification of slice data

The cultured SCN slice data from neonate and adult mice (both wild-type and knockout) were analyzed. First, cellular signals $\{x_i(t) : i = 1, 2, \ldots, N_c; t = 1, 2, \ldots, M\}$ were extracted from the regions of interest in the bioluminescence image (Fig. 5). The number of the cells and the data length were $(N_c, M) = (126, 155), (87, 143), (97, 136), (63, 199)$ for neonate wild-type, adult wild-type, neonate knockout, and adult knockout mice, respectively. The extracted signals were then analyzed by the chi-square periodogram (significance level of 1 %) [2]. Average and standard deviation of the estimated periods were summarized in Table S1 (neonate wild-type: $N = 126$, adult wild-type: $N = 78$, neonate knockout: $N = 97$, adult knockout: $N = 22$).

To quantify the level of synchrony among cellular signals of the slice, the cellular phases were estimated by the Cosinor's method [3]. The phase ϕ_i of the i-th cell was determined by fitting a cosine function $a * \cos(2\pi(t + \phi_i)/\tau)$ to the cellular signal $\{x_i(t) : t = 40, 41, \ldots, 60\}$, where a is an oscillation amplitude and τ is the average period previously estimated. The phase estimate ϕ_i with the coefficient of determination larger than 0.5 was considered reliable. Standard deviation of the phases of individual cells, which measures the coherence structure, was summarized in Table S1 (neonate wild-type: $N = 126$, adult wild-type: $N = 66$, neonate knockout: $N = 97$, adult knockout: $N = 5$). Extended variations of the phase distributions in adult slices are observed in both experiment and model. The averaged periods are also in good agreement except those of the neonate knockout slice. Although the period is shortened in the experiment, it is elongated in the model. The elongated period of the model might be due to the coupling delay, which lengthened the feedback loops of individual cells. The cause of the shortened period observed in the experiment is not well understood.

4 Hopf bifurcation of the single cell model

To identify the transition from damped oscillations to self-sustained oscillations, a bifurcation diagram was drawn. In the single cell model of Eqs. 7-18, the parameter values P_1 generate self-sustained oscillations [4], whereas P_2 give rise to damped oscillations [5]. By changing the oscillator strength α ($0 \leq \alpha \leq 1$), which interpolates the two parameter sets as Eq. 19, local maximum of the Y_1 value was plotted in Fig. S4a. The onset of self-sustained oscillations was observed around $\alpha = 0.5$. To see the bifurcation type, the largest eigenvalue of the Jacobian matrix of the model was simultaneously computed and plotted in Fig. S4b. At the onset point, the real part of the eigenvalue, which is negative before the onset, touches the zero line, while the imaginary part exists, implying the Hopf bifurcation.
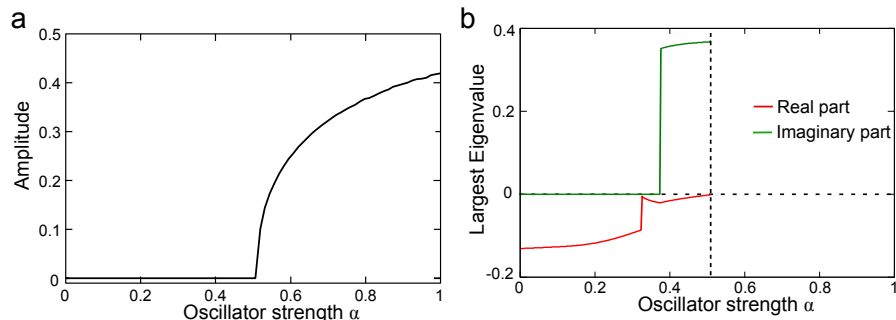
Figure S4: **a**: Dependence of the oscillation amplitude of the single cell model on oscillator strength α. **b**: Largest eigenvalue computed simultaneously with **a** from Jacobian matrix of the single cell model (red: real part, green: imaginary part). At oscillation onset around $\alpha = 0.5$, real part of the complex eigenvalue crosses the zero-line, implying Hopf bifurcation.

5 Dependence of network dynamics on system parameters

To study dependence of the network dynamics on system parameters, we systematically varied the single cell oscillator strength $\alpha \in [0,1]$, the coupling strength $K \in [0,1.5]$, and its delay $\psi \in [0,24]$. The degree of synchrony was quantified by the synchronization index R defined by Eq. 6. In Fig. 6a, the delay was fixed to $\psi = 0$, while the other two parameters were varied. In Fig. 6b, the coupling strength was fixed to $K = 1$, while the other two parameters were varied. In Figs. S5, a and b, period length of the simulated network was drawn in 2-dimensional diagrams corresponding to Figs. 6, a and b. For each cell, the individual period was computed by the chi-square periodogram (significance level of 1 %) [2] and their periods were averaged to represent the network period.

As seen in the blue regions of Fig. S5, small oscillator strength ($\alpha < 0.5$) dampens rhythmicity and sets the network period to zero. The coupling strength K recovers the rhythmicity even in the region, where individual cells are damped oscillators (Fig. S5a). In this region, a clear synchronization among the neurons is observed (Fig. 6a). This agrees quite well with the earlier study that damped single cells are easy to synchronize with each other and that the synchronization recovers rhythmicity of the damped cells [6, 5]. Large coupling strength K increases the synchronization index further.

The timing of coupling described by ψ also has a very strong effect on synchronization. As indicated in Figs. 6b and S5b, a small change in ψ can easily destroy synchronization. Of particular note is the blue region of Fig. S5b, where the synchronization-induced rhythmicity was broken and consequently the individual cells became damped oscillators again.

We mark in Figs. 6 and S5 the parameter settings used to reproduce experimental data (see Fig. 7). Oscillator strength of $\alpha = 0.3$ and $\alpha = 0$ correspond

to wild-type and knockout mice, respectively. Coupling strength of $K = 1$ describes slice culture data well, whereas small coupling strength of $K = 0.2$ represents dispersed culture data. Since an increase of ψ from zero to 12 h deteriorates synchronization, the timing of coupling was changed from neonate ($\psi = 0$) to adult ($\psi = 1$) during the development.
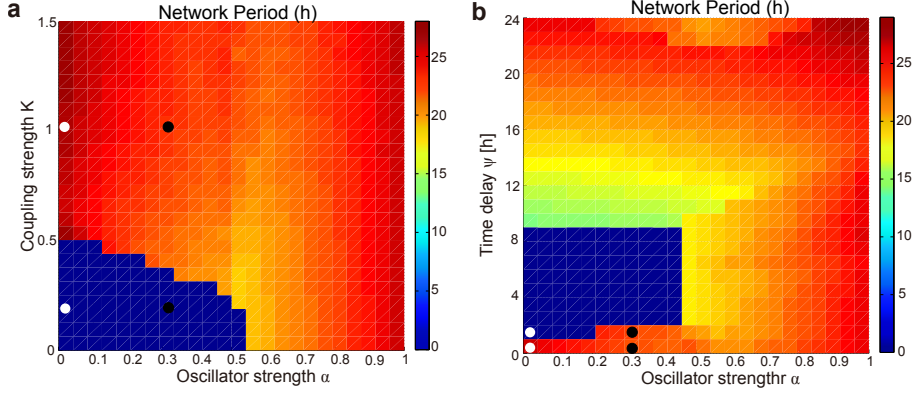

Figure S5: Oscillator network period in the simulated SCN for different choices of system parameters. **a**: Dependence of the period of the cellular network model on oscillator strength α and coupling K. The white and black points indicate conditions for simulating double knockout and wild-type mice, respectively. **b**: Dependence of the period of the cellular network model on oscillator strength α and coupling delay ψ (coupling strength was set to $K = 1$).

6 Entrainment of network dynamics to external stimuli

The entrainment region of Fig. 9 was drawn by varying the Zeitgeber intensity L_0 and Zeitgeber period T. For each combination of (L_0, T), the network (Eqs. 7-18) with external stimuli (Eq. 20) was simulated. By analyzing time series data of Y_1-variable averaged over all cells by the chi-square periodogram (significance level of 1 %) [2], period length of the cellular network was quantified. If the network period is the same as the Zeitgeber period T (difference less than 0.15 h), the network is judged to be entrained to the Zeitgeber.

7 Simulation of actograms

The actogram was drawn by simulating the network dynamics of Eqs. 7-18. At each time, the activity was evaluated by counting the number of cells, Y_1-value of which was above 70 % of its maximum. In the first 15 days of Figs. 8, *c* and *d*, the activity was plotted by applying the external stimuli of Eq. 20, which

8

represents the LD condition. In the following 15 days, the external stimuli were switched off to simulated the activity under DD condition. Then, to quantify the periodicity of the actogram, 5 days length of the activity data (LD data staring from the first day and DD data starting from the 16th day) was analyzed by the periodogram in Fig. S7.

To compare the network model with the experiments, behavioral rhythms in mice from both genotypes are drawn in Figs. 8, a and b, and their periods were analyzed under the same condition as those of the model in Fig. S6.
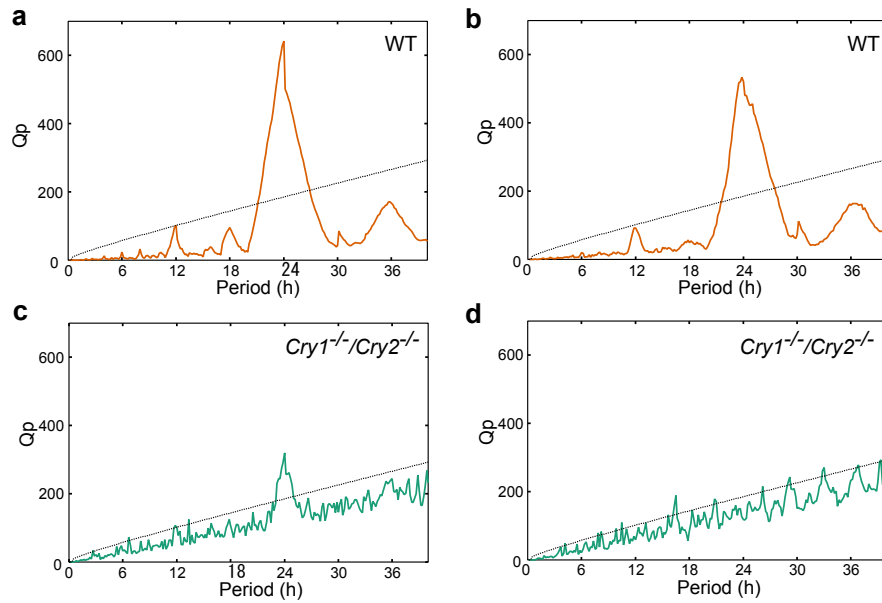

Figure S6: Analysis of behavioral period of mice across both genotypes under different lighting conditions. **a,b**: Chi-square periodogram for wild-type mouse under LD (**a**) and DD (**b**). **c,d**: Chi-square periodogram for $Cry1^{-/-}/Cry2^{-/-}$ knockout mouse under LD (**c**) and DD (**d**).
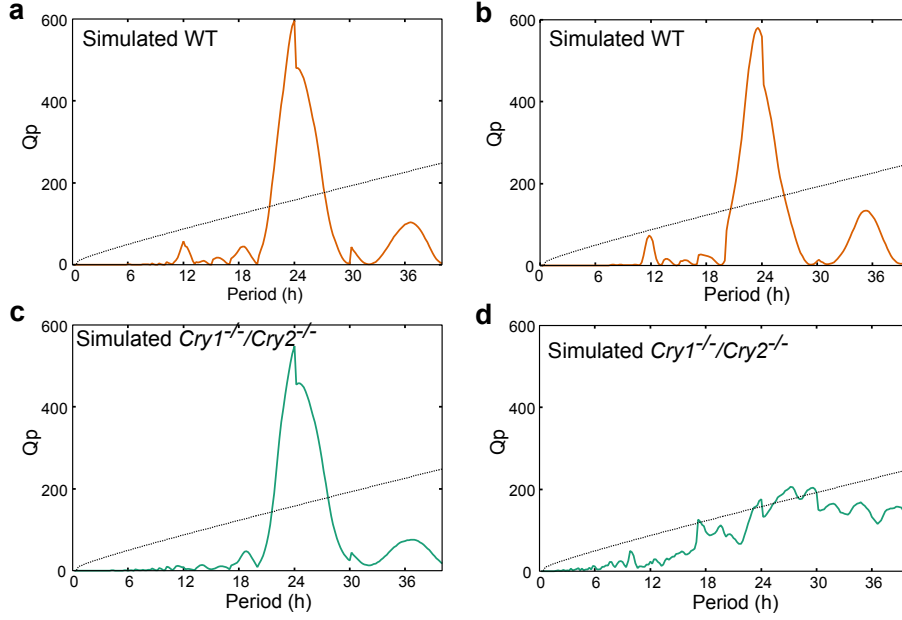
Figure S7: Analysis of period of simulated SCN from both genotypes under different lighting conditions. **a,b**: Chi-square periodogram for simulated wild-type mouse under LD (**a**) and DD (**b**). **c,d**: Chi-square periodogram for simulated knockout mouse under LD (**c**) and DD (**d**).

8 Analysis results of slice culture data

Table S1: Results of the periodicity and phase analysis for slice culture data of neonate and adult mice (both wild-type and knockout). Average and standard deviation of the period estimated by the chi-square periodogram (significance level of 1 %) [2] are indicated. Standard deviation of the phase of individual cells is represented as a quantity to measure the coherence structure. The estimated values are compared with those of the simulated network.

	Mouse	Age	Period	Phase
Experiment	Wild-type	Neonate	24.4±0.5 h	0.13 h
		Adult	25.8±2.8 h	0.64 h
	$Cry1^{-/-}/Cry2^{-/-}$	Neonate	19.0±0.2 h	0.26 h
		Adult	30.8±6.2 h	1.1 h
Model	Wild-type	Neonate	23.0±0.2 h	0.38 h
		Adult	23.9±2.7 h	0.40 h
	$Cry1^{-/-}/Cry2^{-/-}$	Neonate	26.2±0.4 h	0.10 h
		Adult	26.2±7.3 h	1.2 h

9 Parameter settings for the biochemical model

Detailed parameter settings for the biochemical model (Eqs. 7-18) simulated in the main text are summarized in the following tables.

Table S2: Two parameter settings for the biochemical model (Eqs. 7-18): (i) self-sustained oscillator (Becker-Weimann *et al.*, 2004), (ii) damped oscillator (Bernard *et al.*, 2007).

Description	Parameter	Value (Becker-Weimann, 2004)	Value (Bernard, 2007)
Hill coefficient of inhibition of Per/Cry transcription	p	8	3
Nuclear import rate of PER/CRY complex	k_{2t}	0.24 h^{-1}	0.36 h^{-1}
Maximal rate of Bmal1 transcription	v_{4b}	3.6 nM	1.0 nM
Degradation rate of Per/Cry mRNA	k_{1d}	0.12 h^{-1}	0.18 h^{-1}
Degradation rate of cytoplasmatic PER/CRY	k_{2d}	0.05 h^{-1}	0.1 h^{-1}
Degradation rate of nuclear PER/CRY complex	k_{3d}	0.12 h^{-1}	0.18 h^{-1}
Degradation rate of Bmal1 mRNA	k_{4d}	0.75 h^{-1}	1.1 h^{-1}
Degradation rate of cytoplasmatic BMAL1	k_{5d}	0.06 h^{-1}	0.09 h^{-1}
Degradation rate of nuclear BMAL1	k_{6d}	0.12 h^{-1}	0.18 h^{-1}
Degradation rate of nuclear BMAL1*	k_{7d}	0.09 h^{-1}	0.13 h^{-1}

Table S3: Parameter setting of the biochemical model.

Description	Parameter	Value
Hill coefficient of activation of Per/Cry transcription	h	2
No. of PER/CRY complex forming subunits	q	2
Hill coefficient of activation of Bmal1 transcription	r	3
Maximal rate of Per/Cry transcription	v_{1b}	9.0 nM h^{-1}
Michaelis constant of Per/Cry transcription	k_{1b}	1.0 nM
Inhibition constant of Per/Cry transcription	k_{1i}	0.56 nM
Complex formation rate of PER/CRY	k_{2b}	0.3 h^{-1}nM$^{-(q-1)}$
Nuclear export rate of the PER/CRY complex	k_{3t}	0.02 h^{-1}
Michaelis constant of Bmal1 transcription	k_{4b}	2.16 h^{-1}
Degradation rate of Bmal1 mRNA	k_{4d}	1.1 h^{-1}
Translation rate of BMAL1	k_{5b}	0.24 h^{-1}
Nuclear import rate of BMAL1	k_{5t}	0.45 h^{-1}
Nuclear export rate of BMAL1	k_{6t}	0.06 h^{-1}
Activation rate of nuclear BMAL1	k_{6a}	0.09 h^{-1}
Deactivation rate of nuclear BMAL1*	k_{7a}	0.003 h^{-1}
Production constant of transmitter	k_8	1.0 h^{-1}
Degradation rate of transmitter	k_{8d}	4.0 h^{-1}
Activation rate of coupling	k_{x1}	3.0 h^{-1}nM^{-1}
Total concentration of PKA	X_{1T}	15.0 nM
Degradation rate of PKA	k_{dx1}	4.0 h^{-1}
Activation rate of PKA	k_{x2}	0.25 h^{-1}nM^{-1}
Total concentration of CREB	X_{2T}	15.0 nM
Degradation rate of CREB	k_{dx2}	10.0 h^{-1}

10   Additional samples of bioluminescence signals

In addition to bioluminescence signals shown in Fig. 1, *a*, *b*, *d*, and *e*, six more samples are provided here for dispersed SCN cell culture of wild-type and $Cry1^{-/-}/Cry2^{-/-}$ mice. Also from simultaneous plot of the cellular signals in Fig. 5, six indivdual traces are extracted and presented for SCN slice culture of wild-type and $Cry1^{-/-}/Cry2^{-/-}$ mice (both neonate and adult).
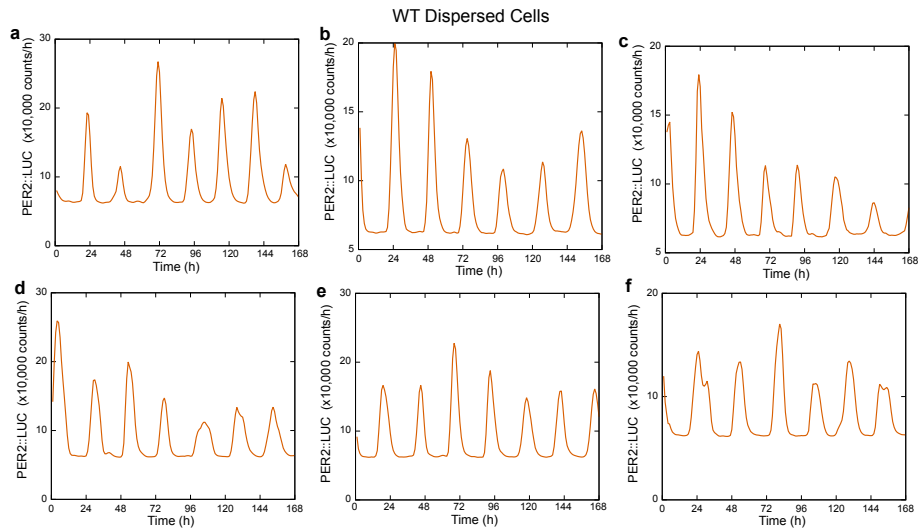
Figure S8: Six samples of bioluminescence signals recorded from dispersed SCN cell culture of wild-type mice.
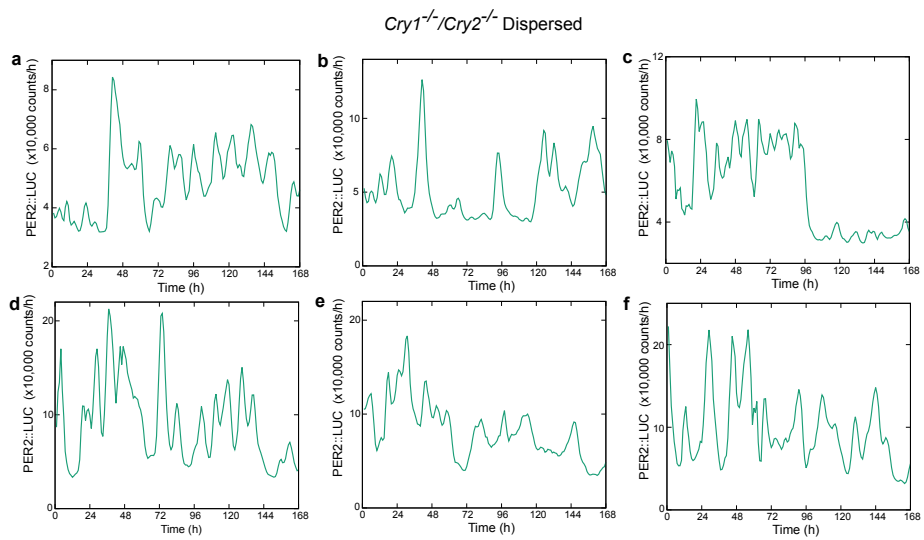

Figure S9: Six samples of bioluminescence signals recorded from dispersed SCN cell culture of $Cry1^{-/-}/Cry2^{-/-}$ mice.
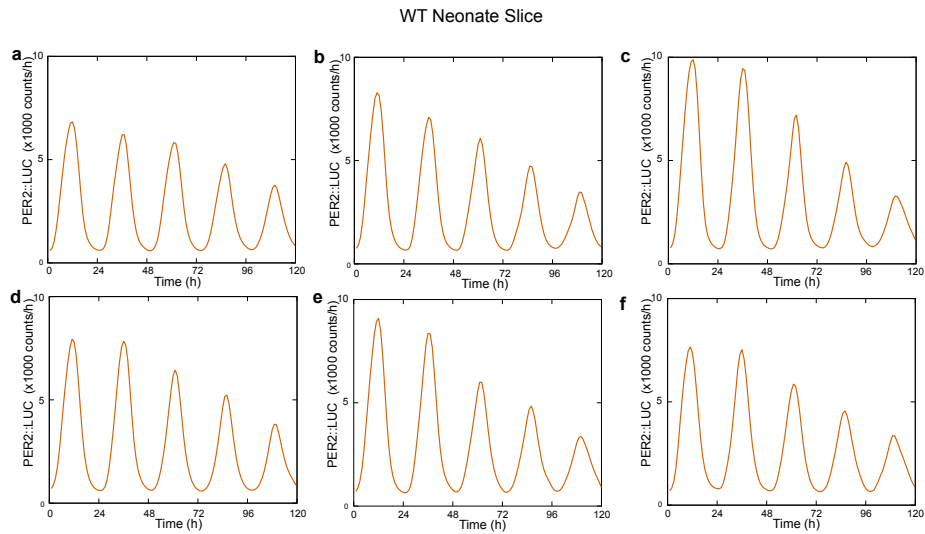
WT Neonate Slice

Figure S10: Six samples of bioluminescence signals recorded from SCN slice culture of WT neonate mice. From simultaneous plot of the cellular signals in Fig. 5a, indivdual traces are extracted in each figure.

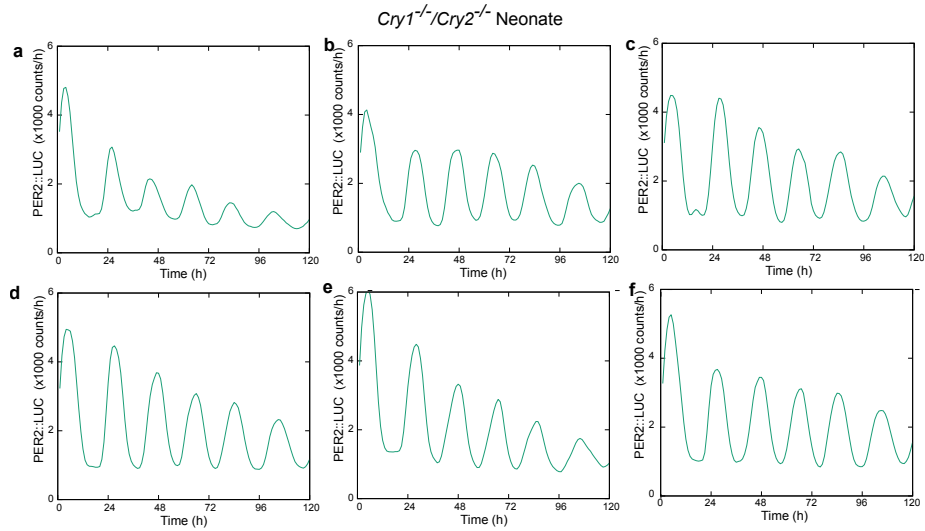$Cry1^{-/-}/Cry2^{-/-}$ Neonate

Figure S11: Six samples of bioluminescence signals recorded from SCN slice culture of $Cry1^{-/-}/Cry2^{-/-}$ neonate mice. From simultaneous plot of the cellular signals in Fig. 5d, indivdual traces are extracted in each figure.
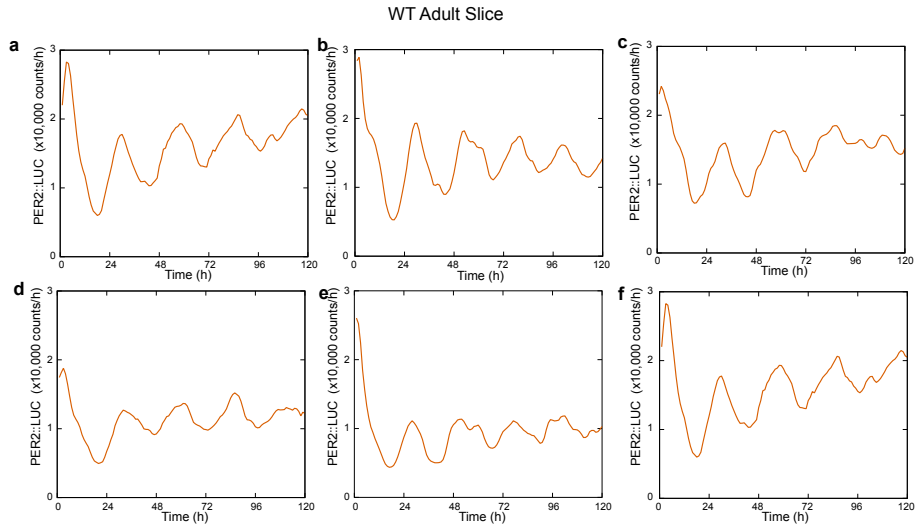
Figure S12: Six samples of bioluminescence signals recorded from SCN slice culture of WT adult mice. From simultaneous plot of the cellular signals in Fig. 5*c*, indivdual traces are extracted in each figure.
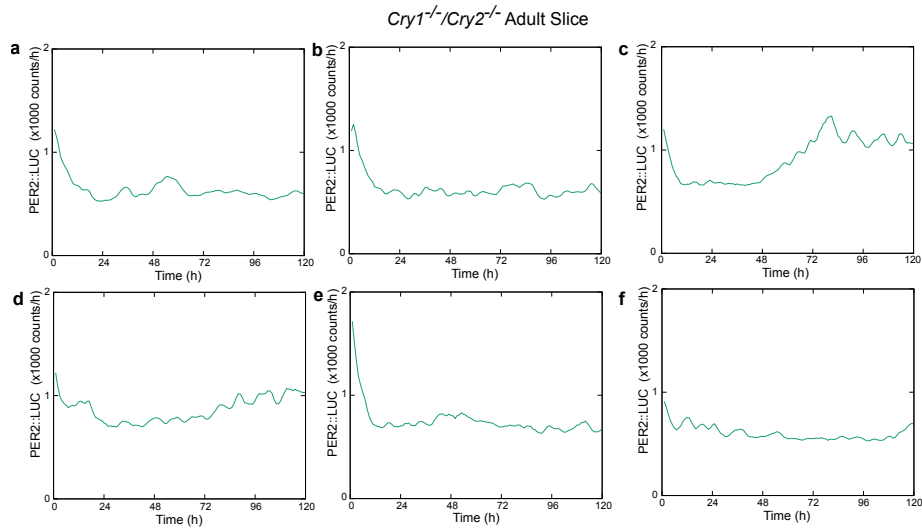

Figure S13: Six samples of bioluminescence signals recorded from SCN slice culture of $Cry1^{-/-}/Cry2^{-/-}$ adult mice. From simultaneous plot of the cellular signals in Fig. 5*e*, indivdual traces are extracted in each figure.

References

[1] Westermark, P. O., D. K. Welsh, H. Okamura, and H. Herzel, 2009. Quantification of Circadian Rhythms in Single Cells. PLoS Comput Biol 5:e1000580.

[2] Sokolove, P. G., and W. N. Bushell, 1978. The chi square periodogram: Its utility for analysis of circadian rhythms. rhythms. Journal of Theoretical Biology 72:131–160

[3] Halberg, F., Y. Tong, and E. Johnson, 1967. Circadian system phase An aspect of temporal morphology; procedures and illustrative examples. In H. von Mayersbach, editor, The Cellular Aspects of Biorhythms, Springer Berlin Heidelberg, 20–48

[4] Becker-Weimann, S., J. Wolf, H. Herzel, and A. Kramer, 2004. Modeling feedback loops of the mammalian circadian oscillator. Biophysical Journal 87:3023–3034.

[5] Bernard, S., D. Gonze, B. Čajavec, H. Herzel, and A. Kramer, 2007. Synchronization-induced rhythmicity of circadian oscillators in the suprachiasmatic nucleus. PLoS Comput Biol 3:e68.

[6] Gonze, D., S. Bernard, C. Waltermann, A. Kramer, and H. Herzel, 2005. Spontaneous synchronization of coupled circadian oscillators. Biophysical Journal 89:120–129.